

POLITECNICO DI TORINO

Master's Degree in Aerospace Engineering



**Politecnico
di Torino**

Master's Degree Thesis

Low-Boom Supersonic Business Jet: Aerodynamic Analysis and Mission Simulation towards a CO₂ Emission Standard

Supervisors

Prof. Nicole VIOLA

PhD. Oscar GORI

PhD. Samuele GRAZIANI

Candidate

Giacomo RICHIARDI

October 2023

Summary

This thesis aims to assess the environmental impact, in terms of CO_2 Metric Value, of the conceptual design of a supersonic business jet, and stands as one of the starting points for evaluating how subsonic regulation can be adapted for future supersonic aircrafts. The work, structured into five different chapters, has been presented at the *AIDAA XXVII International Congress* in Padua on September 5th, 2023.

Introduction The first chapter provides an introductory overview of supersonic civil transport, and the associated main challenges. The focus then narrows onto supersonic business jets, explaining why they are of interest, and presenting a comprehensive review of past and ongoing projects.

Case Study: Low-Boom Business Jet Chapter 2 introduces the aircraft under examination in terms of requirements, preliminary assumptions, configuration and mission profile. The vehicle, designed by some of my colleagues and me from October 2022 to January 2023, is the result of the course *Progetto di Sistemi Aerospaziali Integrati* held by professor Nicole Viola.

Methodology Chapter 3 is the core of the research, since it explains the methodology followed to assess the CO_2 metric value of the case study. To achieve this goal, it is necessary to perform a mission simulation which, in turn, is based on an aerodynamic database. Therefore, Chapter 3 is divided into three key sections:

- **Aerodynamic Analysis:** this section provides the theoretical foundation of fluid flow and details the computational fluid dynamic analysis conducted on the aircraft. In particular, this section presents the numerical mesh grid, obtained using *Ansys ICEM CFD*, and the simulations setting, thanks to *Ansys Fluent* used as pre-processor and solver, exploiting the computational power provided by HPC POLITO (<http://hpc.polito.it>).
- **Mission Simulation:** building upon the aerodynamic analysis and a propulsion database developed by Francesco Piccionello [1], this section elucidates the

mission simulation approach. The simulation is executed using the *ASTOS* software and is the key to the environmental impact assessment.

- *CO₂ Metric Value Assessment*: this final section provides, in line with *ICAO Annex 16 Vol III* [2], a detailed explanation of the *CO₂ Metric Value Assessment*, and the key quantities involved in the calculation.

Results Chapter 4 presents the outcomes of the research and, in line with Chapter 3, is organized into three sections:

- Aerodynamic results;
- Mission simulation results;
- *CO₂ Metric Value* results.

Conclusion and Future Works This concluding chapter summarizes results and findings, and outlines potential future directions.

Acknowledgements

To my Family,

because your sacrifices, understanding, and trust in me have been, and will be, the driving force behind this, and all future achievements. I will always be grateful for your love and guidance.

To my girlfriend Madalina,

because your love, patience, and continuous encouragement have been a constant source of strength. You will always set an example and a point of reference for me.

To all my friends,

to those I have known for ten years and those I met here at the university, because each of you, in your own way, has contributed to this achievement. My door will always be open to you.

To my supervisor Prof. Nicole Viola,

because you offered me different and unique opportunities that helped me lay the foundations of my new path. I will be forever grateful for your mentorship.

To my Co-Supervisors Oscar and Samuele,

because your support and guidance were essential during this research. To both of you, I wish the very best for the future.

Table of Contents

List of Tables	VIII
List of Figures	IX
Acronyms	XIII
1 Introduction	1
1.1 Brief history of supersonic transport	1
1.2 Main challenges of supersonic flight	5
1.2.1 Drag as a function of speed	5
1.2.2 Mitigation of the sonic boom	6
1.2.3 Environmental issues of high speed aircraft	7
1.3 Focus on Supersonic Business Jets	11
1.3.1 Overview of some recent <i>SSBJs</i> programs	14
2 Case study: Low-boom business jet	17
2.1 Requirements and preliminary assumptions	17
2.2 Configuration and mission profile	24
2.2.1 Configuration	24
2.2.2 Mission Profile	27
3 Methodology	29
3.1 Aerodynamic Analysis	30
3.1.1 Theoretical foundations of Fluid Flow	30
3.1.2 CFD analysis	36
3.2 Mission Simulation	46
3.3 CO_2 Metric Value	48
3.3.1 CO_2 emissions evaluation metric value	48
3.3.2 Specific Air Range - <i>SAR</i>	49
3.3.3 Reference Geometric Factor - <i>RGF</i>	50

4 Results	52
4.1 Aerodynamic results	52
4.2 Mission simulation results	63
4.3 CO_2 Metric Value results	67
5 Conclusions and future developments	72
Bibliography	76

List of Tables

1.1	Chronological list of studies on supersonic business jets	12
2.1	Requirements	17
2.2	Database of aircraft studied	19
2.3	Aircraft main data	27
3.1	Part mesh setup	39
3.2	Test Matrix: definition	45
3.3	Other input data for <i>ASTOS</i>	47
4.1	Test Matrix: definition	52
4.2	Test Matrix: results	54
4.3	Test Matrix: updated results	55
4.4	Test Matrix: viscous results	59
4.5	Mass-points and <i>SAR</i> values as in Annex 16 equations	67
4.6	Reference equations variation	68
4.7	Mass-points and <i>SAR</i> values at cruise condition	68
4.8	<i>CO₂ MV</i> results	71

List of Figures

1.1	Supersonic aircraft progress (Source: [4])	2
1.2	<i>Concorde</i> flying at supersonic speed (Source: [9])	3
1.3	Drag coefficient vs Mach number (Source [11])	5
1.4	Sketch of near and far field shock wave patterns (Source: [13])	6
1.5	Sketch of a N-wave (Source: [15])	7
1.6	CO_2 emissions from Int. Aviation, 2005 to 2050 (Source: [2])	8
1.7	Projection of CO_2 emissions from aviation (Source: [19])	9
1.8	Five forecast scenarios of annual emissions of CO_2 and <i>non</i> – CO_2 (Source: [2])	10
1.9	CO_2 emissions per segment and range (Source: [19])	11
1.10	Expected size of the SSBJs market (Source: [25])	13
1.11	<i>Aerion AS2</i> (Source: [5])	14
1.12	<i>QSST-X</i> (Source: [28])	14
1.13	<i>Spike S-512</i> (Source: [29])	15
1.14	<i>HyperMach SonicStar</i> (Source: [30])	15
1.15	<i>NASA Quesst X-59</i> (Source: [32])	16
2.1	Near-field pressure components and ground boom signatures of <i>NASA X-59 QueSST</i> (Source: [34])	19
2.2	Life-cycle benefits due to biofuels (Source: [36])	20
2.3	Volumetric fuel consumption (Source: [37])	21
2.4	Volumetric fuel consumption (Source: [37])	21
2.5	Engine type vs Mach number (Source: [39])	22
2.6	Low by-pass turbofan mixed flow scheme (Source: [38])	22
2.7	Examples of 3500 <i>km</i> radius routes (Source: [40])	23
2.8	Interiors of the aircraft	23
2.9	<i>NASA QueSST X-59</i> sized orthogonal projection (Source: [41])	24
2.10	Case study: orthogonal projection	25
2.11	Case study: isometric overview	25
2.12	Primary structural components of the aircraft	26
2.13	Mission profile: altitude and Mach number	28

3.1	Subsonic and supersonic domains	38
3.2	Above view of the aircraft - geometry	40
3.3	Below view of the aircraft - geometry	40
3.4	Above view of the aircraft - mesh	40
3.5	Below view of the aircraft - mesh	40
3.6	Right-side view of the aircraft - geometry	40
3.7	Left-side view of the aircraft - geometry	40
3.8	Right-side view of the aircraft - mesh	40
3.9	Left-side view of the aircraft - mesh	40
3.10	Front view of the aircraft - geometry	41
3.11	Rear view of the aircraft - geometry	41
3.12	Front view of the aircraft - mesh	41
3.13	Rear view of the aircraft - mesh	41
3.14	Isometric view of the aircraft - geometry	41
3.15	Detail of an engine's nacelle - geometry	41
3.16	Isometric view of the aircraft - mesh	41
3.17	Detail of an engine's nacelle - mesh	41
3.18	Overview of the imported model	43
3.19	The CO_2 Standard Regulatory Limits (Source: [53])	48
3.20	Subsonic cruise reference points (Source: [54])	49
3.21	RGF cross sectional and longitudinal views (Source: [42])	51
3.22	RGF plan view	51
4.1	Cl vs α	57
4.2	Cd vs α	57
4.3	L/D vs α	58
4.4	Cd vs Cd_{visc}	60
4.5	L/D vs L/D_{visc}	60
4.6	Cd vs Cl	61
4.7	Cd vs Cd_{visc}	61
4.8	Cm vs α	62
4.9	Cmy_{cg} vs α	62
4.10	Altitude and Mach performances	63
4.11	Total and propellant mass performances	64
4.12	Angle of attack performance	64
4.13	Efficiency performance	65
4.14	Thrust and drag performances	65
4.15	Range performance	66
4.16	Mass-points as in Annex 16 equations	67
4.17	Mass-points at representative cruise condition	68
4.18	Instantaneous SAR	69

4.19	<i>RGF</i> evaluation: maximum width	69
4.20	<i>RGF</i> evaluation: cabin length	70
4.21	CO_2 metric value	70

Acronyms

AIDAA

Associazione Italiana Di Aeronautica e Astronautica

SST

Supersonic Transport

STAC

Supersonic Transport Aircraft Committee

SCR

Supersonic Cruise Research

VCE

Variable Cycle Engine

HSR

High Speed Research

HSCT

High Speed Civil Transport

HISAC

High Speed Aircraft

JAXA

Japan Aerospace Exploration Agency

NEXST

National Experimental Supersonic Transport

ATAG

Air Transport Action Group

SAF

Sustainable Aviation Fuel

AIAA

American Institute of Aeronautics and Astronautics

QSST

Quiet Supersonic Transport

NASA

National Aeronautics and Space Administration

Quesst

Quiet supersonic technology

CFD

Computational Fluid Dynamic

CAV

Cruise and Acceleration Vehicle

CM

Control Mass

CV

Control Volume

FT

Fischer and Tropsch

Chapter 1

Introduction

This first chapter provides an introductory overview of supersonic transport. It starts with an historical overview of the evolution of supersonic flight, and subsequently delves into the core challenges inherent to the subject, such as the influence of drag in relation to speed, the mitigation of the sonic boom, and the emerging environmental considerations associated with high-speed operations. Then, the discussion focuses on Supersonic Business Jets (*SSBJs*) as the aircraft category studied below, presenting an examination of recent developments in *SSBJ* programs.

1.1 Brief history of supersonic civil transport

Brigadier General Charles E. (Chuck) Yeager made history on October 14, 1947, when became the first man to fly faster than the speed of sound aboard his *Bell X-1* [3]. From 1947 onwards, several supersonic aircraft were built for military use and as technology demonstrators: notable examples include the Soviet *Mikoyan-Gurevich MiG-19* and *MiG-21*, the British *English Electric Lightning*, the French *Dassault Mirage III*, and the American *North American F-100 Super Sabre* and *McDonnell F-101 Voodoo*.

Three different projects emerged in the 1960s with the aim of making supersonic flight a reality also for civil transport, each with a different fate. The U.S. Supersonic Transport (*SST*) program, terminated in 1971 due to concerns regarding economic viability, sonic boom, and environmental issues, the Russian *Tu-144*, which despite achieving flight first in 1968, had a limited service life due to problems such as cabin noise and economic inefficiency, and the British/French *Concorde* [5].

The U.S. *SST* program was initiated in June 1963 when President Kennedy announced a new civil aviation program aimed at creating an aircraft that could travel faster than twice the speed of sound. It led to two competing aircraft designs:

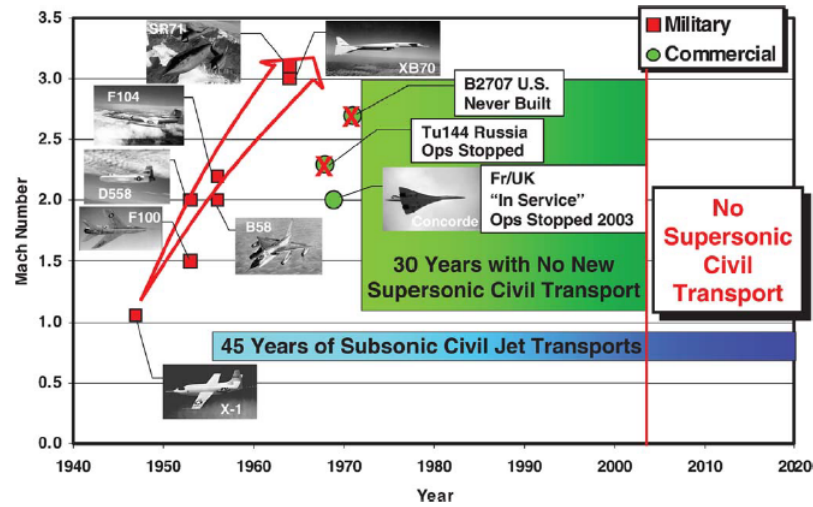


Figure 1.1: Supersonic aircraft progress (Source: [4])

one by *Lockheed* and the other by *Boeing*, as well as two competing engine designs: one by *General Electric* and the other by *Pratt & Whitney*. *Boeing* and *General Electric* emerged as the winners, proposing the *Boeing 2707-100*, a *Mach 2.7*, 300-passenger aircraft with a presumed range of 3500 nautical miles. However, technical challenges arose due to the swing-wing design, which resulted in limited range or payload capacity. As the program progressed, the *Boeing* design transitioned into a fixed-wing, titanium aircraft, similar to *Lockheed's* proposal but, despite the initial enthusiasm, the U.S *SST* program faced several obstacles and was eventually discontinued in May 1971 due to concerns about airport noise, stratospheric impact, political factors, and uncertainties about its economic success [6].

During the development of *Concorde*, the Russians were concerned about falling behind the advancements made by the French and British governments: with the help of a USSR spy, they obtained partial blueprints of *Concorde*, and the task of building the first supersonic passenger aircraft was assigned to chief designer Andrei Tupolev and his team at the Soviet Tupolev design bureau. The *Tupolev Tu-144*, as the Soviet counterpart to *Concorde*, boasted some unique qualities such as excellent aerodynamics, but faced also several issues, including airframe structure failures, cabin noise, and economic inefficiency. In addition, the journey of *Tupolev Tu-144* took a tragic turn during the Paris Air show in 1973 when a terrible crash occurred, resulting in death for 6 crew members and 8 civilians, and the destruction of 15 houses. The aircraft first flew on December 31st, 1968; by 1970 it became the first commercial aircraft to exceed *Mach 2* and then acted as supersonic passenger aircraft from 1977 to 1978 [7].

The *Concorde*'s development originated from separate research efforts in Britain and France focused on supersonic transport, which came after the successful introduction of the turbojet-powered *Comet* aircraft. In Britain, the Supersonic Transport Aircraft Committee (*STAC*), on November 5, 1956, acknowledged that the American *Douglas DC-8* and *Boeing 707* would likely dominate the subsonic market for commercial aircraft, leaving the only option to pursue supersonic flight [6]. In 1962, the British and French governments reached an agreement to jointly develop a supersonic transport aircraft, thus the formation of the *Aérospatiale-BAC Concorde* company. The *Concorde* enjoyed a successful initial period, catering to high-end travelers and becoming a symbol of prestige and technological progress. However, economic challenges, high operational costs, and strict noise regulations limiting its flight overland affected its profitability. Additionally, the tragic crash of *Air France Flight 4590* in July 2000, caused by debris on the runway, raised safety concerns and, after years of debate over the aircraft's future, *British Airways* and *Air France* announced the retirement of *Concorde* in 2003 [8].

In figure 1.2 a famous picture of the aircraft taken in April, 1985, is presented.



Figure 1.2: *Concorde* flying at supersonic speed (Source: [9])

Despite decades of stagnation in supersonic transport, research in this area has persisted.

After learning from the failures of the previous *SST* program, *NASA* took on the responsibility of establishing the technology base for a viable supersonic cruise airplane: the Supersonic Cruise Research (*SCR*) program and the Variable Cycle Engine (*VCE*) program were conducted from 1971 to 1981. In the late 1980s,

feasibility studies for the next-generation *SST* were initiated, resulting in the launch of the High-Speed Research (*HSR*) program in 1989, including in-depth studies and *Tu-144* flight tests in 1995, aiming to develop a 300-passenger, Mach 2.4 supersonic airliner called the High-Speed Civil Transport (*HSCT*). Once again, however, the program was terminated in 1999 due to environmental challenges and budgetary issues.

In Europe, a next-generation supersonic program was initiated in 1994, but it was halted around the same time as the *HSR* program because the focus shifted onto large subsonic airplanes. However, the program High-Speed AirCraft (*HISAC*), also known as "environmentally friendly High-Speed AirCraft", was conducted from 2005 to 2009 to research the technology base for a small-size environmentally friendly supersonic transport.

In Japan, the Japan Aerospace Exploration Agency (*JAXA*) started the National Experimental Supersonic Transport (*NEXST*) project in 1996 to establish advanced design technologies for the next-generation *SST* but it was terminated in 2007 [5].

1.2 Main challenges of supersonic flight

Supersonic flight refers to the movement of an object through the air at a speed exceeding the local velocity of sound. The speed of sound, also known as *Mach* 1, varies depending on atmospheric pressure and temperature: for instance, at sea level and a temperature of $15^{\circ}C$, sound travels at approximately 1225 km/h [10].

Flying at supersonic speed presents unique technical challenges that go beyond those of subsonic flight; some of these are presented below.

1.2.1 Drag as a function of speed

When flying through a fluid like air, each aircraft encounters drag. However, when flying in the supersonic regime, this force becomes more significant, thus a more challenging situation for the propulsive system.

The aerodynamic performance of an aircraft is often assessed by comparing the overall drag D it generates with the lift L it produces, resulting in the lift to drag ratio L/D ; a higher ratio indicates better aerodynamic performance and longer range when other factors, such as aircraft weight and engine performance, remain constant. However, as the Mach number increases, the lift to drag ratio decreases, resulting in reduced range for supersonic aircraft, due to the surge in drag, compared to their subsonic counterparts.

Drag is characterized by a drag coefficient C_D which represents the drag divided by air density, the reference surface, and the square of the vehicle's speed. As presented in figure 1.3, the drag coefficient increases rapidly with Mach number, peaking just above *Mach* 1.

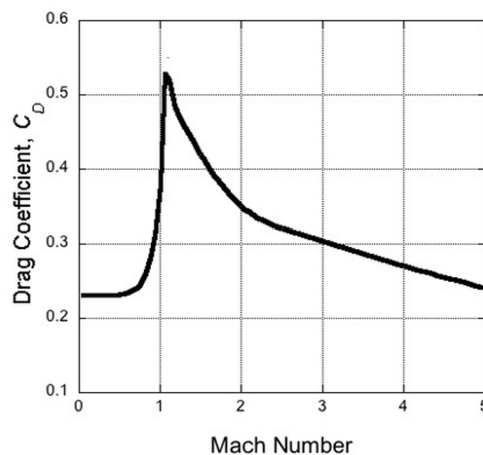


Figure 1.3: Drag coefficient vs Mach number (Source [11])

In addition, as an aircraft enters supersonic speeds, the compressibility of air leads to the formation of shockwaves, which cause sudden changes in pressure, temperature, and density in the flow over the aircraft. These shockwaves generate the characteristic sonic boom associated with the overflight of supersonic aircraft. Moreover, shockwaves contribute to an additional form of drag known as wave drag, becoming the primary source of drag as Mach number exceeds the speed of sound [12].

1.2.2 Mitigation of the sonic boom

When an object travels faster than the local speed of sound, it creates a shock wave system; the series of shock waves eventually merge into a bow and tail shock at a significant distance from the vehicle, as presented in figure 1.4.

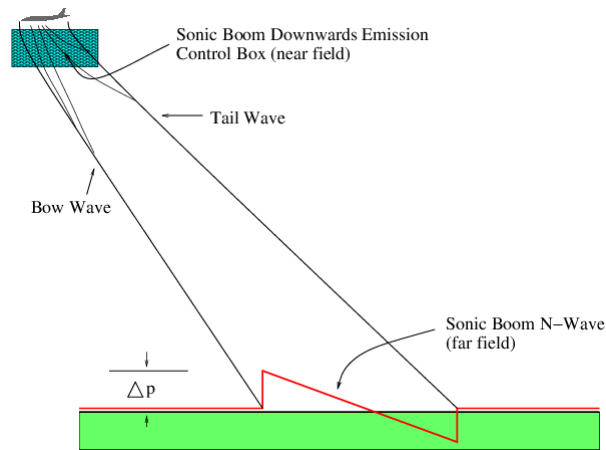


Figure 1.4: Sketch of near and far field shock wave patterns (Source: [13])

At the bow wave, compression occurs, and following this initial compression, there is an approximately linear expansion wave, causing the local pressure to drop below atmospheric pressure. Finally, a second compression wave, or tail shock, restores the pressure back to the atmospheric level. In most cases, the two compression waves have similar intensities, and the expansion wave remains approximately linear. This type of wave system is known as the *N-wave* due to its shape, and it moves continuously with the aircraft during supersonic flight. The ground area affected by this wave system, known as the sonic boom carpet, depends on flight conditions and aircraft characteristics. The duration of the sonic boom Δt affects how a listener perceives it on the ground. If $\Delta t > 0.15$ seconds, the human ear can distinguish two separate booms, thus more discomfort [14].

In figure 1.5 is presented a focus on the N-wave.

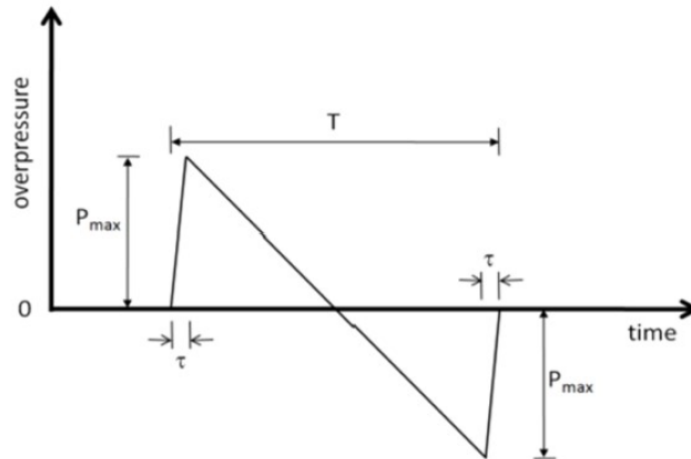


Figure 1.5: Sketch of a N-wave (Source: [15])

With reference to figure 1.5, it must be understood that it is both important to minimize the Δp , in order to have a less intense sonic boom, and to limit the time extension of the N-wave, in order to hear, from ground, only one boom instead of two. At worst, pressure fluctuations from supersonic flight can potentially cause damage to people or buildings on the ground. In addition, the mental impact of the sudden shock experienced by people on the ground has been shown to be unacceptable to significant portions of the public [16].

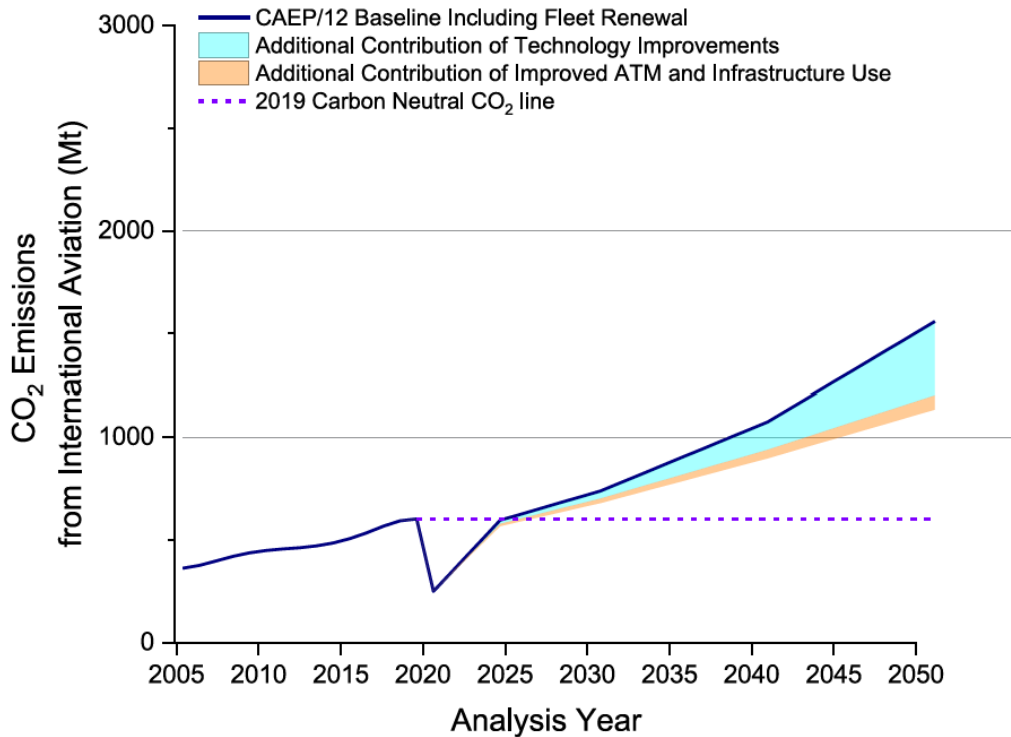
After the power of *Concorde*'s sonic boom became widely known, many countries restricted supersonic flight over land, usually allowing supersonic flight only up to a designated *cutoff* Mach number, while the United States imposed a complete ban on supersonic civil flight [17].

This restriction is still effective to this day and the regulation states as follow: *anyone is prohibited from operating a civil aircraft at a true flight Mach number greater than 1 over land and from a certain distance off shore where a boom could reach the shores* [18].

1.2.3 Environmental issues of high speed aircraft

The aviation sector currently releases more than 600 million tons of carbon dioxide, and this number is expected to more than double by 2050 due to the growth in population and prosperity, as presented in figure 1.6. As a consequence, decarbonization has become one of the most critical challenges of our time.

The Green Deal, introduced by the European Commission in December 2019, sets the challenging objective of achieving net carbon neutrality across all sectors of *EU* member states by 2050. This target, as shown in figure 1.7, is even more



Note: Results were modelled for 2005, 2006, 2010, 2015 (Prior CAEP work cycles), 2018, 2020, 2024, 2030, 2040, and 2050 (CAEP/12).

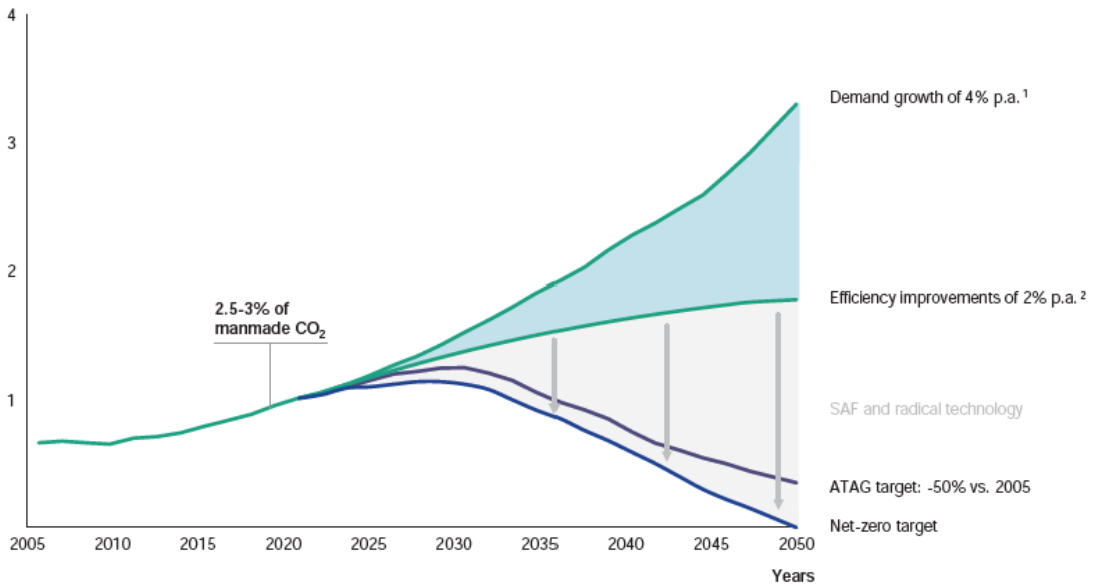
Figure 1.6: CO_2 emissions from Int. Aviation, 2005 to 2050 (Source: [2])

ambitious than those outlined by the Air Transport Action Group (*ATAG*), which aims for carbon-neutral growth from 2020 onwards, and a 50 percent reduction in emissions by 2050 compared to 2005 levels. The aviation sector faces increasing pressure to rapidly decarbonize due to these ambitious goals.

It is important to remember that, while CO_2 emissions are the most widely understood and commonly used metric to measure aviation's climate impact, other emissions play a crucial role as well. In fact, in addition to CO_2 , aircrafts emit other substances at high altitudes, such as nitrogen oxides (NO_x), water vapor, and soot. Although NO_x remains in the atmosphere for only a few weeks while CO_2 for 50 to 100 years, the former contribute to ozone enhancement, which can have a similar negative impact on the climate as CO_2 emissions. Water vapor also directly affects the climate by reflecting climate-warming radiation, but its effects are about ten times less significant than those of CO_2 emissions and do not persist for long times at high altitudes; nevertheless, as a result of water vapor emissions interacting with soot from conventional combustion and atmospheric particles, there is the formation of contrails and cirrus clouds. The extent of their impact compared to

Projection of CO₂ emissions from aviation

Gt CO₂ emissions from aviation
Does not include compensation schemes



1. Assumption based on growth projections from ATAG, IATA, ICCT, WWF, UN
2. ICAO ambition incl. efficiency improvements in aircraft technology, operations and infrastructure

Figure 1.7: Projection of CO₂ emissions from aviation (Source: [19])

CO₂ emissions is still uncertain, as limited studies have investigated and tested this phenomenon. However, simulations conducted by prominent research institutions suggest that the contrail effect could be comparable in magnitude to CO₂'s climate impact [19].

Currently, there is no universally agreed-upon standard for aggregating the various climate impacts of aviation into a single metric but, despite the uncertainties, it is evident that both CO₂ and *non* – CO₂ emissions significantly contribute to global warming, as presented in figure 1.8.

The possible return of *SST* poses even more challenges regarding environmental and noise pollution, because introducing new vehicles could potentially exacerbate emission levels. Presently, there are no established environmental standards that apply to the development of new supersonic designs, but some recent findings indicate that these aircraft are not likely to meet the current standards for subsonic aircraft. In fact, the most probable configuration representative of a supersonic transport vehicle, was estimated to exceed the limits for nitrogen oxides and carbon dioxide by approximately 40% and 70% respectively and, on average, projected to consume 5 to 7 times more fuel per passenger than subsonic aircraft on representative

Future emissions cause future additional warming, with total warming dominated by past and future CO_2 emissions

(a) Future annual emissions of CO_2 (left) and of a subset of key non- CO_2 drivers (right), across five illustrative scenarios

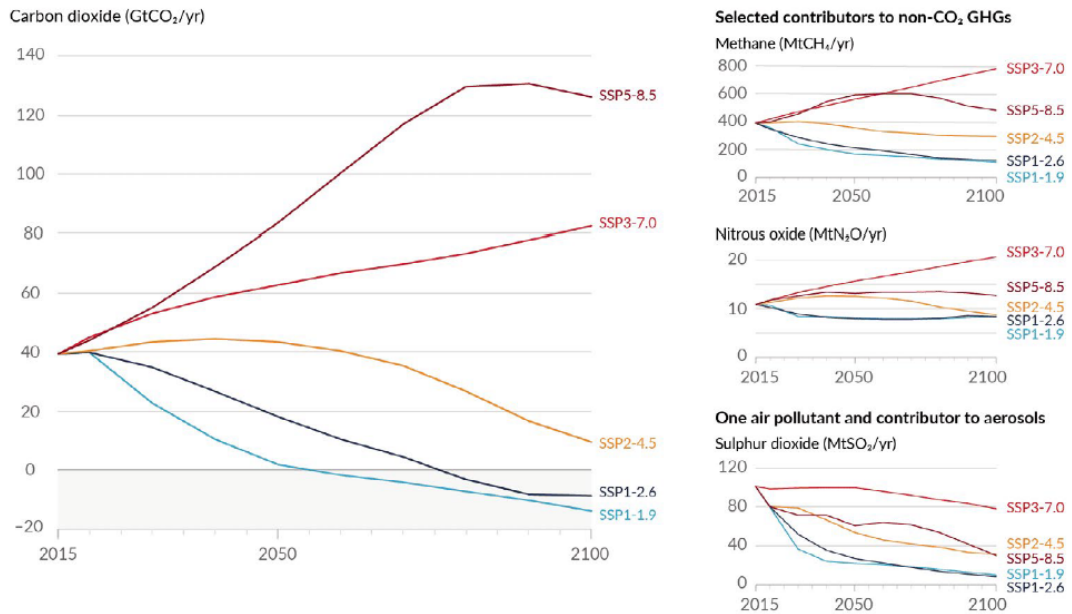


Figure 1.8: Five forecast scenarios of annual emissions of CO_2 and non- CO_2 (Source: [2])

routes. In addition, regarding noise levels, it is suggested that emerging *SSTs* are expected to fall short of meeting even the historical 2006 standard for landing and takeoff noise [20].

Even if it is true that over the last three decades the aviation industry has improved its carbon efficiency on a per-passenger basis with a higher seat density and important technological advancements, the soaring demand for air travel has resulted in a substantial increase in direct CO_2 emissions from aviation. In addition, the projected growth in population and prosperity is expected to further elevate demand, with estimates ranging from 3 to 5 % annually until 2050. Even if efficiency improvements accelerate to the targeted rate of 2 percent per year, as set by the *ICAO*, aviation emissions will still double by 2050. It is therefore evident that additional decarbonization measures will be necessary, including short-term adoption of new fuels such as Sustainable Aviation Fuels (*SAF*) [19].

1.3 Focus on Supersonic Business Jets

Looking at figure 1.9 it is evident how the primary contributors to current aircraft emissions are short, medium, and long-range routes.

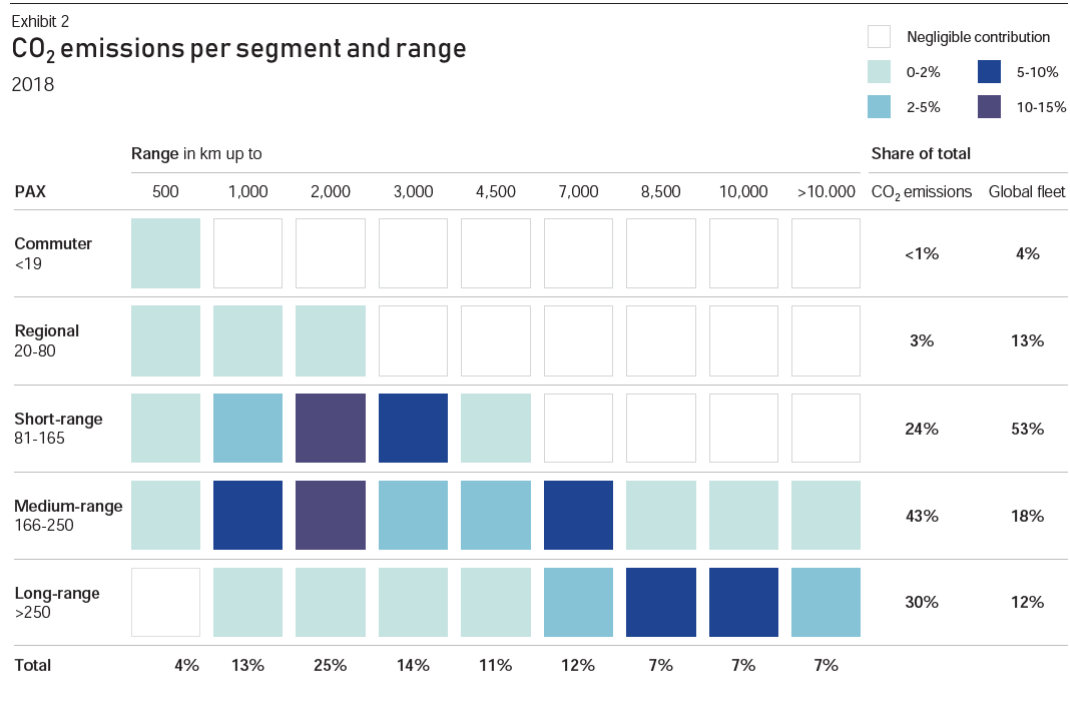


Figure 1.9: CO₂ emissions per segment and range (Source: [19])

Specifically, short-range aircrafts account for approximately one-third of the emissions, as they make up about 53% of the global fleet and contribute to 24% of carbon dioxide emissions. On the other hand, medium and long-range aircraft have a smaller presence in the global fleet, but contribute more to CO₂ emissions, accounting for 43% and 30% respectively. Assessing together short and medium range flights, it can be stated that they are responsible for two-thirds of the current aircraft emissions (67%), constituting about 71 % of the global fleet. The remaining emissions arise from long-range flights with over 250 passengers, served by around 12 percent of the global fleet, and regional and commuter flights which together account for less than 5 percent of emissions, despite being served by approximately 17 percent of the aircrafts. In addition, analyzing flight ranges it is clear that, flights above 7000 kilometers contribute to over 20 percent of emissions, despite constituting less than 5 percent of the total number of flights. In contrast, flights covering less than 3,000 kilometers, regardless of aircraft size, account for over 50

percent of the total aviation CO₂ emissions and represent 90 percent of all flights.

Based on just this data, it becomes apparent that the primary focus of decarbonization efforts in aviation should be on short-range aircraft operating within the range of 2000 to 3000 kilometers, because this category holds the most significant potential for reducing emissions and achieving sustainability goals.

In addition, after conducting studies over the last decades, it became clear that, in order to take the first initial step towards a new era of supersonic transport, due to the increasingly strict noise requirements regarding sonic boom, it turned out to be necessary to develop small and quiet supersonic jets, whose potential customers include corporate flight departments, government agencies, private individuals, charter companies, and fractional companies [5].

In table 1.1 is summarized a chronological list of all industries and research centers which conducted a comprehensive study about the future market of supersonic business jets.

Future market of <i>SSBJs</i>		
Meridian International Research	1999	Source: [21]
Gulfstream	2003	Source: [4]
Aerion Corporation	2005	Source: [22]
Teal Group	2007	Source: [23]
Deutscher Luftund Raumfahrtkongress	2011	Source: [17]
NASA	2011	Source: [24]

Table 1.1: Chronological list of studies on supersonic business jets

As stated above, even if for the most of air travellers a low price airline is still necessary, there is a specific subset of passengers which accord paramount importance to time, thus the feasibility studies of supersonic business jets. In fact, the utilization of business aircrafts yields substantial time savings, and renders irrelevant the hassles of lengthy check-ins, security protocols, and congested airport delays. These aircraft extend their appeal through their versatile operational adaptability, provision of safety measures, and an environment that nurtures social connections, making them a "flying-office" and often leaving an indelible impression on business partners or guests. Furthermore, owners have the freedom to navigate to any destination at their discretion, making possible even mid-flight adjustments to the course.

The figure 1.10 was used by Welge, C.Nelson, and J.Bonet during the 28th *AIAA Applied Aerodynamics Conference* in Chicago to illustrate the passengers'

willingness to pay and the level of service demanded, suggesting a potential market gap for small-size supersonic aircraft.

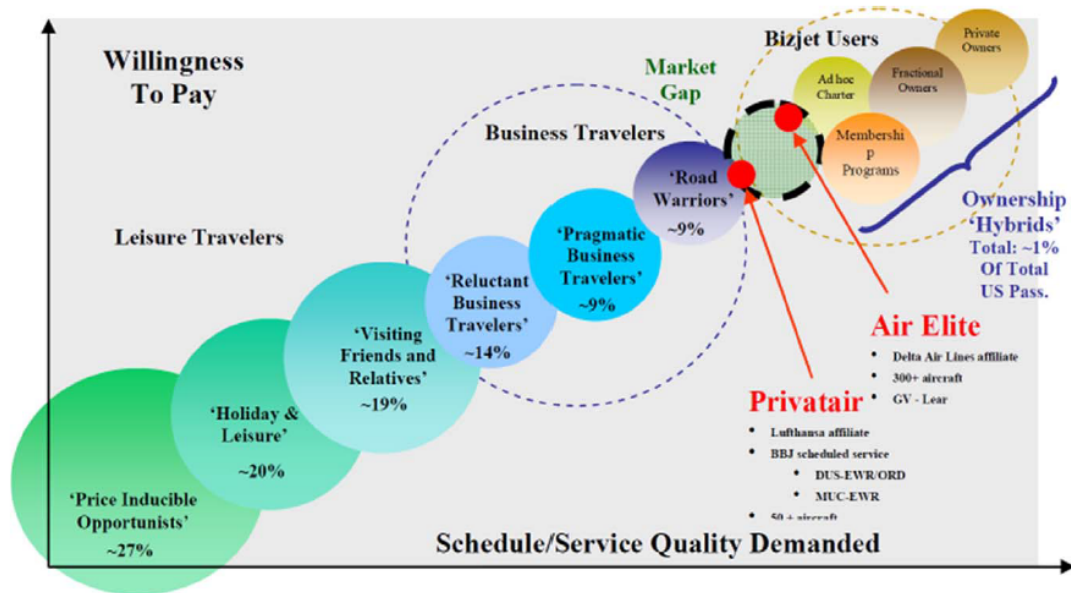


Figure 1.10: Expected size of the SSBJs market (Source: [25])

The interest in supersonic civil transport finds its roots not only in profit motives but also in the important role that technology itself plays. The ability for planes to fly at supersonic speeds has been around for a long time, and there have been big improvements since the *Concorde* era. However, there's still work to be done and issues to be solved, thus the curiosity that leads men to always go further.

In the following subsection a brief overview of the existing *SSBJs* programs is presented.

1.3.1 Overview of some recent *SSBJs* programs

Aerion Corporation

The USA-based Aerion Supersonic was established in 2004 and later formed a partnerships with *Lockheed Martin* and *GE Aviation*; it firstly held significant promise, however, ceased operations in May 2021 without ever creating a prototype of its *AS2*, presented in figure 1.11, due to difficulties in securing the necessary new funding to advance its aircraft into production [26].



Figure 1.11: *Aerion AS2* (Source: [5])

Supersonic Aerospace International

Established in 2001, the mission of the *Supersonic Aerospace International*, with his *CEO* Michael Paulson, was to craft a 21st-century Quiet Supersonic Transport (*QSST*), distinguished by its "quiet supersonic" technology. The *QSST-X*, presented in figure 1.12, presents an advanced double delta wing design, distinguished by its inverted V-tail, studied in collaboration with *Lockheed Martin*; however, due to lack of funds and internal disagreements, the company went dormant in 2010 [27].



Figure 1.12: *QSST-X* (Source: [28])

Spike Aerospace

Headquartered in both Boston, MA, and Florida, Spike Aerospace is a company launched in 2013 and currently driving the advancement of supersonic aviation with its *Spike S-512*, presented in figure 1.13. The aircraft is claimed to be simultaneously quiet, efficient, eco-friendly, yet luxury and fast [5].



Figure 1.13: *Spike S-512* (Source: [29])

HyperMach Aerospace

Established in 2008 in Los Angeles, HyperMach Aerospace, with its SonicStar presented in figure 1.14, was a company that claimed to be able to achieve Mach 4 flight while remarkably minimize the sonic boom. In addition, as a testament to their commitment to sustainability, the company entrusted SonicBlue to develop the hybrid electric turbine engines [5] but, as of today, the company's website no longer exists.



Figure 1.14: *HyperMach SonicStar* (Source: [30])

NASA Quesst X-59

With a commitment to advancing knowledge and enhancing aviation, NASA has been engaged for decades in researches aimed at mitigating sonic boom noise, a central obstacle to achieving overland supersonic flight. In 2016, the National Aeronautics and Space Administration commenced a project with the objective of creating a demonstrator aircraft for low-boom flight, aiming to achieve a flight-measured sonic boom loudness of 75 PLdB or lower. For this purpose, they chose *Lockheed Martin* as the contractor responsible for designing and fabricating the aircraft named the *X-59* (figure 1.15). The *Quesst* mission, which stands for Quiet Supersonic Technology, involves the construction of the *X-59* and, following initial flight tests to verify the aircraft's adherence to design specifications, different supersonic flights over various communities. This extensive data-gathering endeavor aims firstly to gauge public perceptions of the sounds emanating from this innovative design, and secondly to verify the acoustic *CFD* predictions [31].



Figure 1.15: *NASA Quesst X-59* (Source: [32])

Chapter 2

Case study: Low-boom business jet

In this chapter, the focus shifts onto the case study, which lays the foundations of this thesis work. In fact, the following project results from the development of an high speed civilian aircraft, at a conceptual design stage, belonging to the *CAV* category, air-breathing cruise and acceleration vehicle. It was developed from October 2022 to January 2023 as part of the academic course *Progetto di Sistemi Aerospaziali Integrati*, held by Professor Nicole Viola at Politecnico di Torino, by some of my colleagues and me.

The following chapter is structured into two primary sections: initially, the attention is directed towards the requirements and initial considerations that laid the groundwork for the design, then the focus is on the aircraft configuration and mission profile.

2.1 Requirements and preliminary assumptions

The main requirements to be met are presented in table 2.1.

Requirements	
Sonic Boom	$\Delta p_{MAX, cruise} < 1.5 \text{ psf}$
Propellant	Biofuel
Cruise Mach number	1.5
Range	$> 3500 \text{ km}$
Payload	8-12 passengers

Table 2.1: Requirements

In order to meet these stringent requirements and to frame the main issues, some preliminary assumptions have been stated in the very first phase of developing, so as to have guidelines around which the aircraft design was articulated.

- **Sonic Boom** - In order to determine the configuration of the aircraft, a reference model has to be chosen, and the criteria to identify the best geometry shall be based on the most relevant requirement: the low boom. To minimize this effect it is important to imagine an aircraft equipped with a long spike projecting forward from the leading edge of a slender fuselage, designed to minimize the cross-section area [33]. The sonic boom can be described by the distribution of pressure generated by the aircraft while it's moving at a supersonic speed. The pressure field that originates around the aircraft is called near field. It propagates through the atmosphere and reaches the ground, typically with a N-shape profile which is called far field. In order to minimize the sonic boom, it is necessary to minimize both the increment of pressure and the time distance between the peaks reaching the ground (< 0.15 s), so that observers only hear one boom and not two, each one corresponding to a peak of pressure.

For this purpose, the function describing the near field needs to be as smooth as possible. The variation of pressure is proportional to the function F , which is described by the following equation [34]:

$$F(x) = \frac{1}{2\pi} \int_0^x \frac{A_e''(\bar{x}, \theta)}{\sqrt{x - \bar{x}}} d\bar{x} \quad (2.1)$$

x is the body coordinate of the aircraft from the nose on its symmetry plane and A_e'' is the equivalent area, which is obtained through a sum of a contribution due to the lift, and one due to the cross section of the aircraft intersected by a Mach plane.

An evaluation of far and near field's signatures of the vehicles presented in table 2.2 shows that the best configuration is given by the *NASA X-59 QueSST* [34].

Figure 2.1 shows the F function and its contributions of lift and volume. Moreover, the volume function smoothness shows that the wave drag is minimised as well, according to the area rule. A good usage of volumes and lift allows for an optimal near field through the juxtaposition between the positive peaks of the function F caused by the lift, and the negative ones caused by the volume.

The maximum peak of pressure that reaches the ground is moderate and the period of time between the positive maximum overpressure and the negative one satisfies the requirement.

Aircraft studied by Y. Sun and H. Smith

BOOM Airliner
 Aerion AS-2
 Spike S-512
 HyperMach SonicStar
 Cranfield E-5 SSBJ
 NASA X-59 QueSST

Table 2.2: Database of aircraft studied

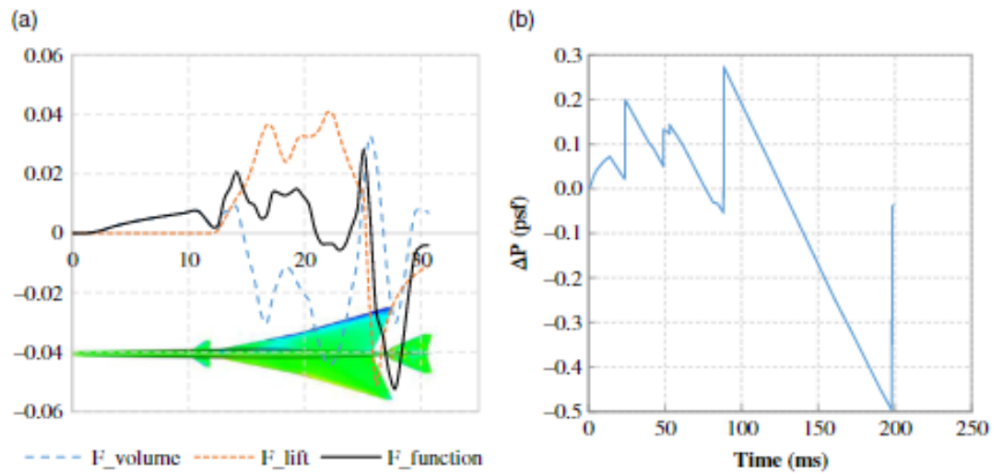


Figure 2.1: Near-field pressure components and ground boom signatures of *NASA X-59 QueSST* (Source: [34])

- **Propellant** - Given the proven need for new fuels and propulsion technologies to seek solutions to improve the environmental and societal impacts of air transport, if, on the one hand, the implementation of new propulsion technologies may be harder to achieve in the early next few years, the use of new fuels such as Sustainable Aviation Biofuels - *SAF* may be the solution to efficiently start our path towards net-zero emissions.

The great advantage of biofuels, among other *SAFs*, is represented by the fact that they are the so called *drop-in* fuels, meaning that they can be immediately used in regular existing propulsion systems without any changing in the aircraft's infrastructure; in addition, biofuels are made 100% from renewable waste and residue raw materials, have similar properties to conventional jet fuels and, among all, as presented in figure 2.2, can reduce the life cycle greenhouse gas

emissions drastically compared to conventional jet fuels [35].

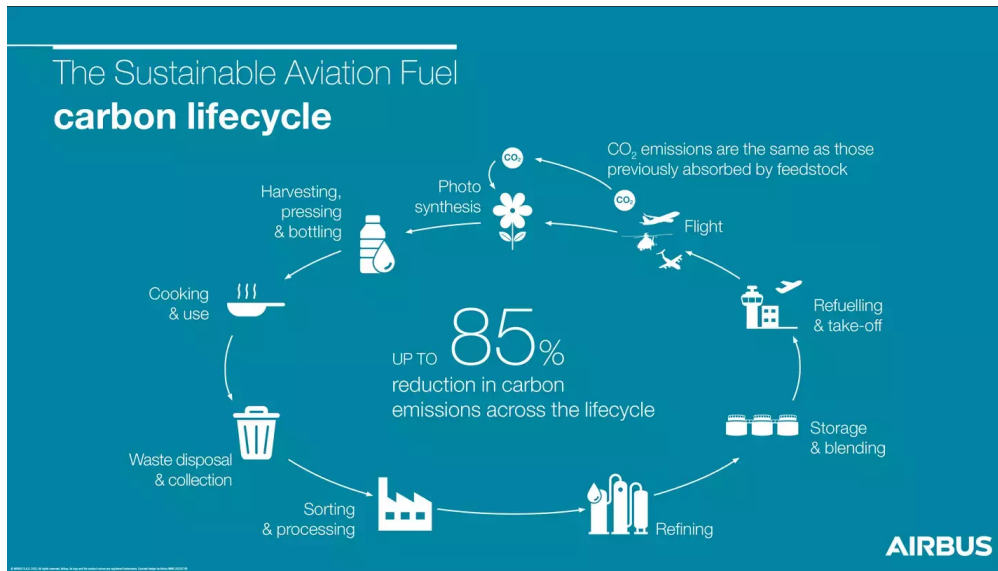


Figure 2.2: Life-cycle benefits due to biofuels (Source: [36])

This aircraft uses 100% *FT-SPK/A*. *FT-SPK/A* is a variation of another *SAF* called *FT-SPK*, which is based on the gasification of biomass in a gas composed by hydrogen and carbon monoxide. This gas is then catalytically converted to a liquid hydrocarbon fuel blending component in the *Fischer and Tropsch* reactor. Depending on the type of catalyst and range of temperatures, this process can produce hydrocarbons like methane or products with more carbon atoms. Usually the main catalysts used in *FT* reaction are iron, cobalt, nickel, and ruterium. In order to obtain *FT-SPK/A* some aromatic compounds are added to *FT-SPK*. *FT-SPK/A* has the highest density compared to other *SAFs* ($805.2 \text{ km}/\text{m}^3$), due to his aromatic compounds, thus a lower volumetric fuel consumption as presented in figure 2.3; in addition, *FT-SPK/A* maintains its energy properties almost unchanged compared to *Jet A1* as shown in figure 2.4. For the operator, *FT-SPK/A* could be the best choice in terms of fuel economy, especially when the cost of fuel is on a volume basis [37].

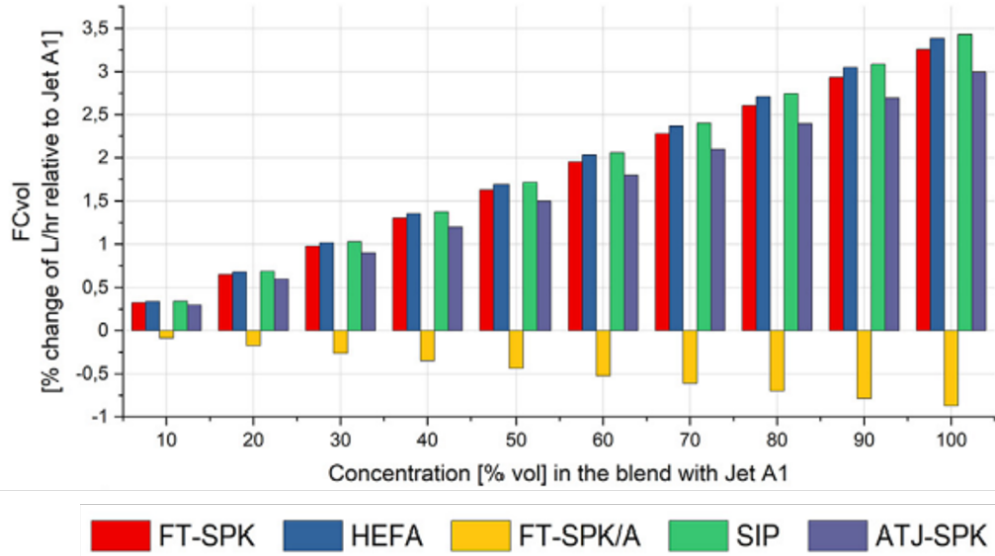


Figure 2.3: Volumetric fuel consumption (Source: [37])

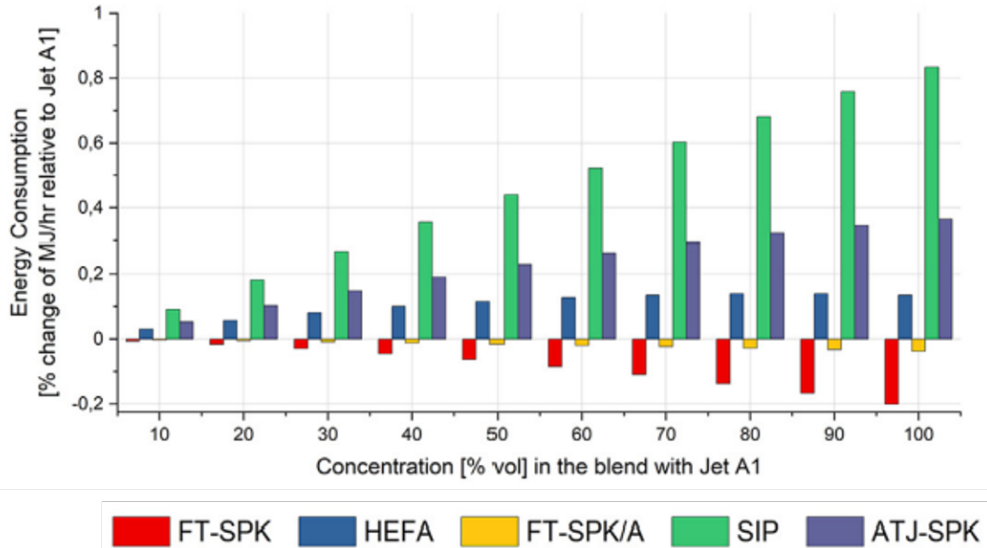


Figure 2.4: Volumetric fuel consumption (Source: [37])

- **Cruise Mach number** - $M = 1.5$ is a convenient trade off between current subsonic planes and future supersonic *CAVs*, since, as presented in figure 2.5, it implies a supersonic cruise that can be possible with advanced low by-pass ratios turbofan engines, without the use of a post-combustor, so as to minimize the emissions of both pollutant and noise [38].

Following the innovation trend of this project, it was decided to focus on

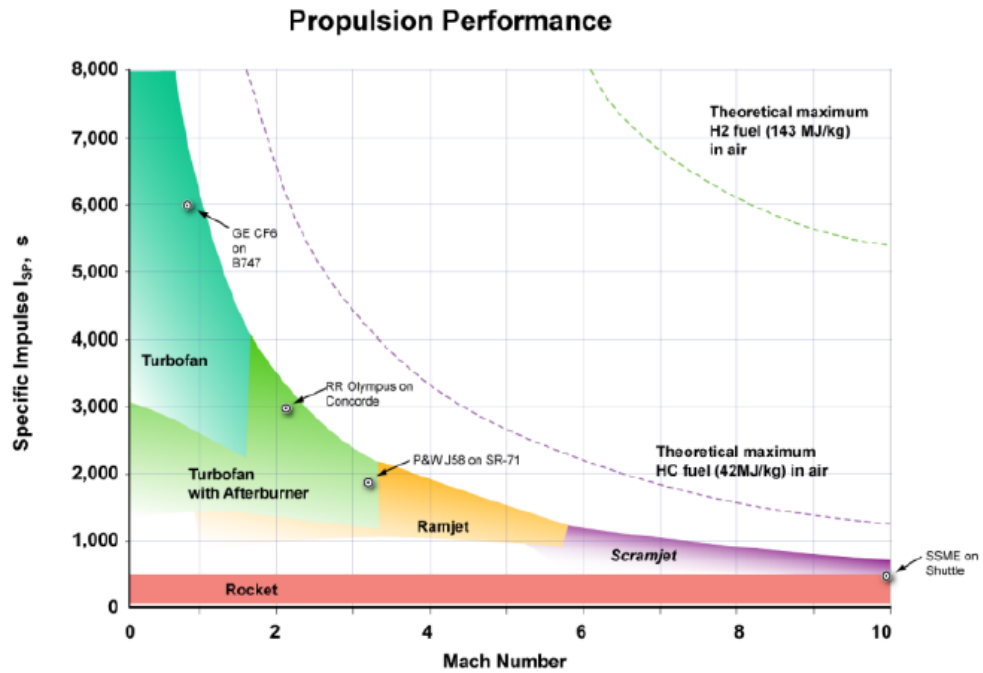


Figure 2.5: Engine type vs Mach number (Source: [39])

conceptual engines. This aircraft is equipped with two state of the art turbofan engines, each characterised by an inlet diameter of 1.1 m , by-pass ratio of 0.75 and overall-pressure ratio of 28, carefully modelled by Francesco Piccionello as part of his master thesis project [1]. A scheme of one engine is presented in figure 2.6.

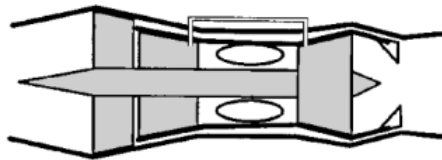


Figure 2.6: Low by-pass turbofan mixed flow scheme (Source: [38])

- **Range** - Range above 3500 km was chosen so as not to be too stringent a parameter for the realisation of the mission. Even though existing business jet have a range of about 3500 nm ($\sim 6500\text{ km}$), since the course was focused on the development of on-board systems, there was no time to optimise the aircraft by simultaneously studying different configurations in order to choose the best one, and this optimisation is beyond the scope of this thesis. In spite

of this, making a short to medium-range aircraft is in line with what was mentioned above, because this category holds the most significant potential for reducing emissions and achieving sustainability goals. In any case, providing a 3500 km route still allows the aircraft user a high degree of flexibility, as demonstrated below. Figure 2.7 shows 3500 km radius circles centred in Turin, Dallas, Tokyo and Sydney as examples.

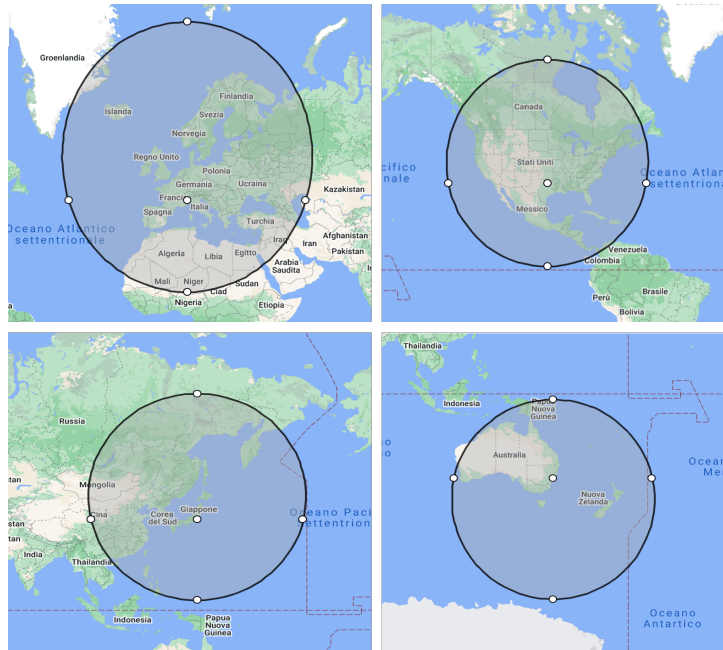


Figure 2.7: Examples of 3500 km radius routes (Source: [40])

- **Payload** - In line with existing business jets, this configuration hosts 12 passengers in a business configuration, and the designed interiors are presented in figure 2.8.



Figure 2.8: Interiors of the aircraft

2.2 Configuration and mission profile

2.2.1 Configuration

Given the low-boom assumptions mentioned above, the sketch of the aircraft is based on *NASA QueSST X-59*, but some modifications were applied in order to satisfy the requirements. The first change was introduced because of the most important design requirement: the payload. In fact, the central part of the fuselage was made longer and wider in order to host 12 passengers comfortably. To dimension this part, a seat pitch of 1.4 metres was assumed. This change in geometry generated a gap between the leading edge of the root chord of the wing, and the cockpit, which were originally at the same x coordinate from the front of the vehicle, as presented in figure 2.9. This had a beneficial effect because it allowed the placement of the passengers' entrance door.

Another modification consists in the location of the engines. Due to the necessity of having two thrusters, the only one already present was moved from the tail, under the vertical stabilizer, to the wing, so as to avoid an accumulation of weight that would have moved the centre of gravity backwards, reducing the stability. These two changes brought to a forward translation of the centre of gravity, allowing for a bigger aerodynamic moment that the elevator can generate. Then, the possibility to remove the canard winglets had to be taken into account, but it was decided to keep them in order not to change the reference geometry.

In figure 2.9 is presented the geometry of the *NASA QueSST X-59*, while in figures 2.10 and 2.11 are presented respectively a sized orthogonal projection of the aircraft studied, and an isometric overview.

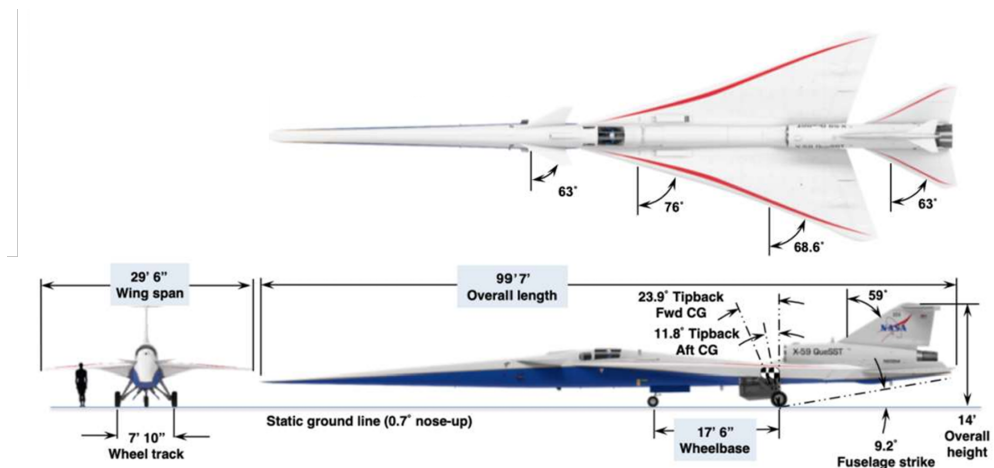


Figure 2.9: *NASA QueSST X-59* sized orthogonal projection (Source: [41])

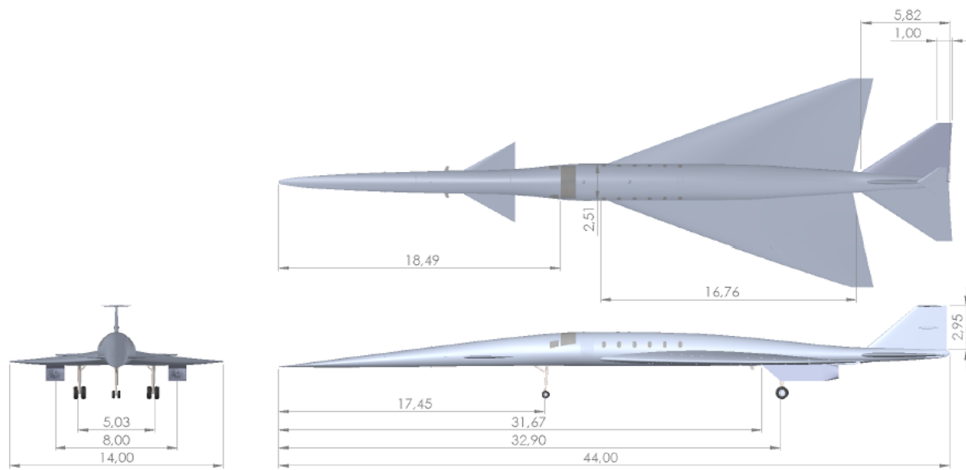


Figure 2.10: Case study: orthogonal projection



Figure 2.11: Case study: isometric overview

Once the aircraft shape was defined and its key components were positioned, the primary structural elements were integrated, as presented in figure 2.12.

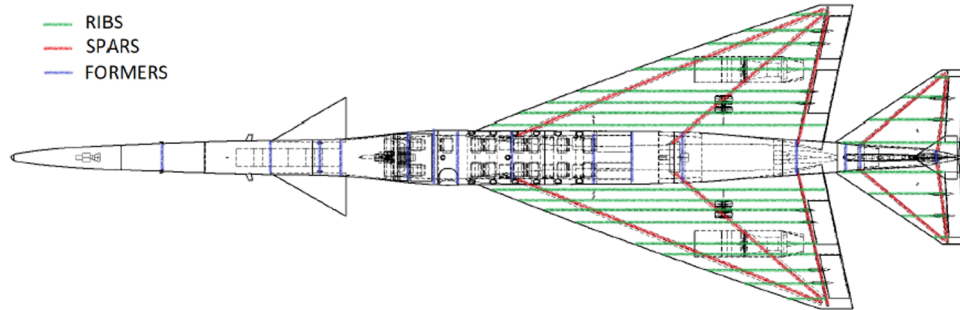


Figure 2.12: Primary structural components of the aircraft

It was decided to distribute the spars following an homothetic pattern and placing them at approximately 15%, 60%, and 90% of the local chord. This arrangement leads to excessive stiffness to the outer regions but is sufficient for a preliminary definition; further iterations and structural analyses will aim to refine and lighten the wing. Ribs on the wing panels were strategically placed to assist in the even distribution of concentrated loads across the spars and to uphold the airfoil's shape. These ribs were aligned parallel to the aircraft's longitudinal axis and strategically positioned at critical junctures, including areas with flight control system actuators, landing gear, or the engine pylon. Additionally, the wing ribs serve the dual purpose of defining integrated tanks and preventing fuel sloshing, while also maintaining rib weight reduction. In addition, both the horizontal and vertical tails hide two spars, adhering to the same homothetic distribution principle, complemented by key ribs. Main formers, integrated into the fuselage, serve to establish proper load distribution, to link spars and fuselage, and to enhance the structural rigidity in the presence of openings, such as hatches or windows.

The data collected in table 2.3 are the results of the preliminary design of the aircraft. To reach this goal, the *ASTRID* software was used. *ASTRID* is a software designed in-house at the Politecnico di Torino that helps students with aircrafts design, defining both the conceptual design and the detailed design of the various subsystems.

Aircraft main data	
Payload [kg]	1500
MTOM [kg]	39283
Empty weight [kg]	19048

Continued on next page

Aircraft main data	
Fuel mass [kg]	18434
Wing surface [m^2]	112
Wingspan [m]	14
Fuselage diameter [m]	2.2
Length [m]	44
Range [km]	3500
Mach cruise	1.5
Propellant	FT-SPK/A

Table 2.3: Aircraft main data

For this case study, all the systems listed below have been designed and integrated on board:

- Avionic system
- Flight Control system
- Landing Gear system
- Environmental Control system
- Anti/De Icing system
- Propellant system
- Electric Power system

2.2.2 Mission Profile

The aircraft's mission profile is a structured description of the sequence of phases that the plane undergoes from departure to arrival.

Commencing with takeoff, the aircraft initiates its trajectory from ground level, transitioning into a subsonic climb phase. During this initial ascent, it steadily gains altitude until reaching a speed of Mach 0.95 at an altitude of 11 kilometers. Then, the transition to supersonic flight is recorded and the supersonic climb phase starts. The aircraft accelerates to Mach 1.5 at an altitude of 14 kilometres and is ready to start the cruise phase. The cruise is maintained at Mach 1.5 and lasts for approximately 118 minutes; during this time the aircraft climbs from 14 to 17 kilometres. As the mission progresses, the aircraft starts the supersonic descent phase, gradually decelerating to Mach 0.95, while descending to an altitude

of 13 kilometers. Then, the descent continues in a subsonic flight regime for approximately 16 minutes and the aircraft is ready to safely land.

In the following list the main phases of the mission profile are summarized, while figure 2.13 illustrates the mission profile in terms of altitude and Mach number.

- *Take-off and Subsonic climb*: the aircraft is brought at $M = 0.95 @ \sim 11 \text{ km}$;
- *Supersonic climb*: acceleration from $M = 0.95$ to $M = 1.5 @ \sim 14 \text{ km}$;
- *Supersonic cruise*: cruising at $M = 1.5$ for about 118 minutes; the aircraft climbs to $\sim 17 \text{ km}$;
- *Supersonic descent*: deceleration from $M = 1.5$ to $M = 0.95 @ \sim 13.5 \text{ km}$;
- *Subsonic descent and Landing*: the aircraft continues its descent and lands in about 16 minutes.

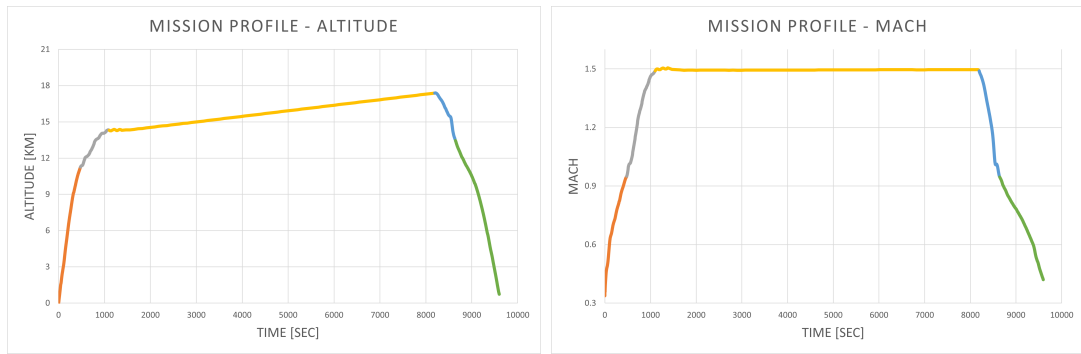


Figure 2.13: Mission profile: altitude and Mach number

Comparing this mission profile to those of other *SSBJs*, the parallels are quite evident in terms of phases, Mach number and altitude. However, it is noteworthy to mention that this mission profile represents an initial iteration and does not encompass out-of-nominal scenarios like missed approaches, loitering, or aborted takeoffs. Subsequent refinements could incorporate these phases to better analyze the aircraft’s performances.

Chapter 3

Methodology

The purpose of this chapter is to explain in detail the working methodology followed in the realisation of this thesis. The integration of three separate sections highlights the in-depth method used to address critical aspects of fluid dynamic characterization, mission simulation, and CO_2 emissions assessment.

The first section deals with the definition of a table, called test-matrix, to characterise the aerodynamic performance of the aircraft and to be used as input for the mission simulation. To do so, starting from the *CAD* model of the aircraft presented previously, a series of fluid-dynamic simulations were carried out using *Ansys ICEM CFD* as a mesh generator, and *Ansys Fluent 2022R2* as pre-processor and solver, exploiting the computational resources provided by HPC@POLITO (<http://hpc.polito.it>). Therefore, several issues that had to be addressed in order to compute the test-matrix are presented.

The aim of the second section is to perform a mission simulation relying both on the aerodynamic data gathered previously, and on a propulsion database generated by Francesco Piccionello as part of his master thesis [1]; the reason for doing so, is the need to find useful information to assess the CO_2 impact of the aircraft. In order to achieve this goal, the *Astos* software, by *Astos Solutions*, was used.

The third section shifts its focus towards quantifying the CO_2 Metric Value for the case study presented before. Since the actual emission standard is defined only for subsonic aircraft (*ICAO Annex 16 Volume III* [42]), the main objective is to support the work towards the definition of a potential CO_2 emission standard for supersonic aeroplanes. Therefore, in the course of this last section, the existing regulations in the assessment of aircraft CO_2 emissions will initially be presented, and an attempt to amend for a supersonic aircraft will be proposed.

3.1 Aerodynamic Analysis

3.1.1 Theoretical foundations of Fluid Flow

Fluids are substances characterized by their lack of resistance to external shear forces, thus the deformation of fluid particles even with the slightest applied force. Even though many macroscopic differences, identical laws of motion govern both liquids and gases. External forces induce the motion in fluids; the former can be categorized as either surface forces, like wind-induced shear above oceans, or body forces, such as gravity. While all fluids respond in similar ways to external forces, their macroscopic properties exhibit substantial variations, with density and viscosity being the primary properties of simple fluids, but also *Prandtl* number, specific heat, and surface tension.

Flow velocity profoundly impacts fluid properties across various regimes, as taken into account by the *Reynolds's* number, a ratio of viscous over inertial forces. At sufficiently low velocities (low *Re*), fluid inertia becomes negligible, while, as velocity increases, inertia becomes significant, resulting in smooth trajectories for fluid particles, or, for further escalation in velocity, in a more chaotic form of flow known as *turbulent flow*.

Moreover, the ratio of flow velocity to the speed of sound in the fluid is an important indicator of the fluid's characteristics, since it influences the mathematical nature of the problem and the approach to finding solutions. For low Mach numbers, $M < 0.3$, the flow is treated as incompressible; otherwise, it's deemed compressible. Subsonic flow occurs when $M < 1$, while supersonic flow when $M > 1$ and hypersonic flow when $M > 5$.

Numerous other factors impact fluid flow, including temperature differentials, leading to heat transfer, density differences, leading to buoyancy effects, and also solute concentration, phase changes, and surface tension, but these effects are generally secondary [43].

In the following, firstly the fundamental equations governing fluid flow, and secondly a focus on numerical solutions are outlined. For further details of conservation principles, see [44].

Conservation Principles

Conservation principles can be established through the examination of a specified amount of material known as a control mass (CM), and its extensive attributes such as mass, momentum, and energy; however for fluid flows, tracing the trajectory of a specific parcel of material becomes difficult. Hence, it is more convenient to

analyze the flow within a defined spatial region, control volume (CV), following the control volume method.

Since the conservation equations governing mass and momentum share common terms, the first focus will be on these two equations.

In the case of mass, which remains constant as it is neither created nor destroyed, the conservation equation takes the form:

$$\frac{dm}{dt} = 0 \quad (3.1)$$

It is clear that the conservation principle establishes a connection between the rate of change of the analyzed property within a designated control mass and externally imposed influences.

On the other hand, momentum is subject to alteration through the impact of external forces, and its governing conservation equation is Newton's second law of motion:

$$\frac{d(m\mathbf{V})}{dt} = \sum \mathbf{f} \quad (3.2)$$

In order to translate these principles in line with the control volume method, the variables under consideration must shift from being extensive properties to intensive properties, so as not to be affected by the quantity of matter examined. For example it can be considered density as mass per unit volume, and velocity as momentum per unit mass.

Following this line of thought, if q is a conserved intensive property and Ω_{CM} is the volume occupied by the CM, the extensive property Q is:

$$Q = \int_{\Omega_{CM}} q d\Omega \quad (3.3)$$

Hence,

$$\frac{d}{dt} \int_{\Omega_{CM}} q d\Omega = \frac{d}{dt} \int_{\Omega_{CV}} q d\Omega + \int_{S_{CV}} q (\mathbf{V} - \mathbf{V}_b) \cdot \hat{\mathbf{n}} dS \quad (3.4)$$

Where S_{CV} is the surface enclosing CV, \mathbf{V} and \mathbf{V}_b are respectively the velocity of the flow and the velocity of S_{CV} and $\hat{\mathbf{n}}$ is the outgoing versor of S_{CV} . This equation shows that the variation rate of the property analyzed within the control mass, corresponds to the variation rate of the property within the control volume, plus the net flux of the property through the boundary of the control volume.

Once that the left hand side of the conservation principle is defined, it is possible to write the integral form of the conservation principle for any scalar quantity

simply considering volume and surface sources of q as follows:

$$\frac{d}{dt} \int_{\Omega} q d\Omega = - \int_S q (\mathbf{V} - \mathbf{V}_b) \cdot \hat{\mathbf{n}} dS + \int_{\Omega} q_v d\Omega + \int_S \mathbf{q}_s \cdot \hat{\mathbf{n}} dS \quad (3.5)$$

Assuming q to be a continuous function and Ω fixed in space, by applying the Gauss' divergence theorem:

$$\int_{\Omega} \frac{\partial q}{\partial t} d\Omega + \int_{\Omega} \nabla \cdot (q \mathbf{V} \cdot \hat{\mathbf{n}}) d\Omega = \int_{\Omega} q_v d\Omega + \int_{\Omega} \nabla \cdot \mathbf{q}_s d\Omega \quad (3.6)$$

If Ω is arbitrary, it is possible to have the differential form of the conservation principle for any scalar quantity:

$$\frac{\partial q}{\partial t} + \nabla \cdot (q \mathbf{V}) \cdot \hat{\mathbf{n}} = q_v + \nabla \cdot \mathbf{q}_s \quad (3.7)$$

Considering now \mathbf{q} as a conservative vector quantity, defined $\bar{\mathbf{F}}_{\mathbf{q}}$ the flow tensor and $\bar{\mathbf{q}}_s$ the surface source tensor, the integral form of the conservation principle for any vector quantity is:

$$\frac{d}{dt} \int_{\Omega} \mathbf{q} d\Omega = - \int_S \bar{\mathbf{F}}_{\mathbf{q}} \cdot \hat{\mathbf{n}} dS + \int_{\Omega} \mathbf{q}_v d\Omega + \int_S \bar{\mathbf{q}}_s \cdot \hat{\mathbf{n}} dS \quad (3.8)$$

If Ω is fixed and arbitrary, it is possible to have the differential form of the conservation principle for any vector quantity:

$$\frac{\partial \mathbf{q}}{\partial t} + \nabla \cdot \bar{\mathbf{F}}_{\mathbf{q}} = \mathbf{q}_v + \nabla \cdot \bar{\mathbf{q}}_s \quad (3.9)$$

Mass conservation Considering $q = \rho$ and no mass sources, the integral form of the continuity equation is:

$$\frac{d}{dt} \int_{\Omega} \rho d\Omega = - \int_S \rho \mathbf{V} \cdot \hat{\mathbf{n}} dS \quad (3.10)$$

It is possible to transform the integral form into the derivative form by applying the Gauss' divergence theorem to the convection term, hence considering infinitesimally small the control volume, obtaining:

$$\frac{\partial \rho}{\partial t} + \nabla \cdot (\rho \mathbf{V}) = 0 \quad (3.11)$$

Momentum conservation Considering $\mathbf{q} = \rho \mathbf{V}$, $\mathbf{q}_v = \rho \mathbf{f}$ (for example gravity per unit volume), and $\bar{\mathbf{q}}_s = \bar{\mathbf{\Pi}}$, the integral form of the momentum equation is:

$$\frac{d}{dt} \int_{\Omega} \rho \mathbf{V} d\Omega = - \int_S \rho \mathbf{V} \mathbf{V} \cdot \hat{\mathbf{n}} dS + \int_S \bar{\mathbf{\Pi}} \cdot \hat{\mathbf{n}} dS + \int_{\Omega} \rho \mathbf{f} d\Omega \quad (3.12)$$

Once again, if Ω is fixed and arbitrary, it is possible to transform the integral form of the momentum conservation into the derivative form, obtaining::

$$\frac{\partial(\rho \mathbf{V})}{\partial t} + \nabla \cdot (\rho \mathbf{V} \mathbf{V}) = \nabla \cdot \bar{\mathbf{\Pi}} + \rho \mathbf{f} \quad (3.13)$$

Keeping in mind that:

$$\bar{\mathbf{\Pi}} = -p \bar{\mathbf{I}} + \bar{\boldsymbol{\tau}} \quad (3.14)$$

Equation 3.13 can be rewritten as follows:

$$\rho \frac{\partial \mathbf{V}}{\partial t} + \rho \mathbf{V} \cdot \nabla \mathbf{V} = -\nabla p + \nabla \cdot \bar{\boldsymbol{\tau}} + \rho \mathbf{f} \quad (3.15)$$

Before proceeding with the energy equation it is important to remember that the momentum equation is a vector equation so, in the Cartesian space, is made by three different equations.

Energy conservation Let us define:

- $E = e + \frac{V^2}{2}$ total energy per mass unit;
- $q = \rho E$ total energy per volume unit;

The integral form of the energy equation is:

$$\begin{aligned} \frac{d}{dt} \int_{\Omega} \rho E d\Omega = & - \int_S \rho E \mathbf{V} \cdot \hat{\mathbf{n}} dS + \int_S (\bar{\mathbf{\Pi}} \cdot \mathbf{V}) \cdot \hat{\mathbf{n}} dS + \dots \\ & \dots + \int_{\Omega} \rho \mathbf{f} \cdot \mathbf{V} d\Omega - \int_S \mathbf{q} \cdot \hat{\mathbf{n}} dS + \int_{\Omega} q_v d\Omega \end{aligned} \quad (3.16)$$

As done before, it is possible to derive the derivative form of the energy equation:

$$\rho \frac{\partial E}{\partial t} + \rho \mathbf{V} \cdot \nabla E = \nabla \cdot (\bar{\mathbf{\Pi}} \cdot \mathbf{V}) + \rho \mathbf{f} \cdot \mathbf{V} - \nabla \cdot \mathbf{q} + q_v \quad (3.17)$$

Navier-Stokes equations From the conservation equations:

$$\begin{cases} \frac{\partial \rho}{\partial t} + \nabla \cdot (\rho \mathbf{V}) = 0 \\ \rho \frac{\partial \mathbf{V}}{\partial t} + \rho \mathbf{V} \cdot \nabla \mathbf{V} = -\nabla p + \nabla \cdot \bar{\boldsymbol{\tau}} + \rho \mathbf{f} \\ \rho \frac{\partial E}{\partial t} + \rho \mathbf{V} \cdot \nabla E = -\nabla \cdot (p \mathbf{V}) + \nabla \cdot (\bar{\boldsymbol{\tau}} \cdot \mathbf{V}) + \rho \mathbf{f} \cdot \mathbf{V} - \nabla \cdot \mathbf{q} + q_v \end{cases} \quad (3.18)$$

Introducing the Newtonian fluid constitutive equation:

$$\bar{\boldsymbol{\tau}} = 2\mu \bar{\mathbf{D}} + \lambda(\nabla \cdot \mathbf{V}) \bar{\mathbf{I}} \quad (3.19)$$

In the case where the rates of expansion/compression are small, namely, in the case of validity of the Stokes hypothesis:

$$\bar{\boldsymbol{\tau}} = 2\mu \bar{\mathbf{D}} - \frac{2}{3}\mu(\nabla \cdot \mathbf{V}) \bar{\mathbf{I}} \quad (3.20)$$

Lastly, taking into account the Fourier's law:

$$\mathbf{q} = -\lambda \nabla T \quad (3.21)$$

It is possible to merge all this information into the balance equations to obtain the Navier-Stokes equations:

$$\begin{cases} \frac{\partial \rho}{\partial t} + \nabla \cdot (\rho \mathbf{V}) = 0 \\ \rho \frac{\partial \mathbf{V}}{\partial t} + \rho \mathbf{V} \cdot \nabla \mathbf{V} = -\nabla p + \nabla \cdot (2\mu \bar{\mathbf{D}} - \frac{2}{3}\mu(\nabla \cdot \mathbf{V}) \bar{\mathbf{I}}) + \rho \mathbf{f} \\ \rho \frac{\partial E}{\partial t} + \rho \mathbf{V} \cdot \nabla E = -\nabla \cdot (p \mathbf{V}) + \nabla \cdot (\bar{\boldsymbol{\tau}} \cdot \mathbf{V}) + \rho \mathbf{f} \cdot \mathbf{V} + \nabla \cdot (\lambda \nabla T) + q_v \end{cases} \quad (3.22)$$

Euler equations In fluid flows occurring far from solid surfaces or characterized by high velocities, the influence of viscosity is typically negligible. If the viscous effects are completely disregarded, thus $\bar{\boldsymbol{\Pi}} = -p \bar{\mathbf{I}}$, the *Navier-Stokes* equations are reduced to the Euler equations. The latter are useful for studying compressible flows at high Mach numbers, bearing in mind that the effects of viscosity and turbulence are important only in a small region near the walls.

The three-dimensional Euler equations, considering an inviscid, compressible, and adiabatic flow, are articulated as follows:

Continuity Equation:

$$\frac{\partial \rho}{\partial t} + \nabla \cdot (\rho \mathbf{V}) = 0 \quad (3.23)$$

Momentum Equations:

$$\rho \frac{\partial \mathbf{V}}{\partial t} + \rho \mathbf{V} \cdot \nabla \mathbf{V} = -\nabla p + \rho \mathbf{f} \quad (3.24)$$

Energy Equation:

$$\rho \frac{\partial E}{\partial t} + \rho \mathbf{V} \cdot \nabla E = -\nabla \cdot (p \mathbf{V}) + \rho \mathbf{f} \cdot \mathbf{V} \quad (3.25)$$

Solving the Euler equations can be difficult; however, since no boundary layer near the walls need be resolved, it is possible to use a coarser grid. For this reason, the simulations over the entire aircraft presented in the following sections have been carried out solving the Euler equations, then adjusting the data via a viscous correction.

3.1.2 CFD analysis

Introduction to *CFD* and components of a numerical solution method

The relations describing fluid flow are partial differential, or integro-differential equations, which are usually not solvable analytically, except under special conditions. In order to achieve an approximate numerical solution, a discretization approach is employed. The discretization process takes a spatial domain and divides it into smaller parts, enabling the application of approximations over these smaller elements. As a result, discrete outcomes are obtained at specific points in space, paving the way for numerical solutions that can be efficiently computed using modern computers. However, it is crucial to emphasize that the accuracy of these numerical solutions hinges heavily on the quality and precision of the employed discretization techniques.

The purpose of this exposition is to explain how the used commercial software work, in order to showcase the work done.

In the following, some of the essential components of a numerical solution method are presented, and, for each one, a detailed study will be undertaken to elucidate what was used/developed to assess the aerodynamic performance of the aircraft presented in the previous chapter.

Mathematical Model

The basis of every numerical technique lies in the mathematical model, a collection of partial differential or integro-differential equations along with their boundary conditions.

The mathematical model explained below has been implemented within the software *Ansys Fluent 2022R2*, and is characterised by [45]:

- Ideal gas law:

$$p = \rho R^* T \quad (3.26)$$

p is the static pressure, ρ is the density, R^* is the specific gas constant and T is the static temperature;

- Calorically perfect gas, i.e. characterised by an univocal relationship between internal energy and static temperature:

$$e = c_v T \quad (3.27)$$

- Compressible flow model for ideal gas:

- The speed of sound in the gas is defined as follows:

$$c = \sqrt{\gamma R T} \quad (3.28)$$

Where γ is the ratio of specific heat: $\gamma = c_p/c_v$

- The ideal gas law, for compressible flows, is written in the form:

$$\rho = \frac{p_{op} + p}{\frac{R}{M_w} T} \quad (3.29)$$

Where p is the local static pressure relative to the operating pressure, p_{op} is the operating pressure defined by the user ($p_{op} \approx 10250 \text{ Pa} @ 16 \text{ km}$), M_w is the air's molecular weight, T is the static temperature (computed from the energy equation) and R is the universal gas constant.

- Inviscid flow model:

- The velocity vector of the flow at the wall must adhere to the tangency condition:

$$\mathbf{v} \cdot \hat{\mathbf{n}} = 0 \quad (3.30)$$

- Euler equation, reformulated in a version better suited to numerical problems [46]:

$$\frac{\partial}{\partial t} \int_V \mathbf{W} dV + \oint \mathbf{F} dA = \int_V \mathbf{H} dV \quad (3.31)$$

Where:

$$\mathbf{W} = \begin{bmatrix} \rho \\ \rho u \\ \rho v \\ \rho w \\ \rho E \end{bmatrix}, \quad \mathbf{F} = \begin{bmatrix} \rho \mathbf{V} \\ \rho u \mathbf{V} + p \mathbf{i} \\ \rho v \mathbf{V} + p \mathbf{j} \\ \rho w \mathbf{V} + p \mathbf{k} \\ \rho E \mathbf{V} + p \mathbf{V} \end{bmatrix}, \quad \mathbf{H} = \begin{bmatrix} 0 \\ 0 \\ 0 \\ 0 \\ E + \frac{p}{\rho} \end{bmatrix} \quad (3.32)$$

The discretization method is the method used to approximate the differential equations by a system of algebraic equations for the variables at some set of discrete locations in space. The discretization method used is the *Finite Volume Methods*.

The solution domain is partitioned into discrete control-volumes using a grid that establishes the boundaries of these control-volumes. A common approach involves defining control-volumes using a suitable grid and associating the computational node with the control-volume center. The integral conservation equation 3.31 is applicable to each individual control-volume, as well as to the entirety of the solution domain. Summing the equations for all control-volumes, it is possible to recreate the conservation equation for the entire system, since surface integrals across inner control-volume faces cancel out.

Numerical Grid

The discrete positions for computing variables are determined by the numerical grid, which is a representation of the geometric domain, and partitions the solution domain into a finite number of smaller regions. The type of numerical grid used for this problem is an unstructured grid, since it is indicated for complex geometries and is capable of conforming to arbitrary solution domain boundaries. In addition, the unstructured grids are particularly well-suited for finite volume methods [43]. The control volumes can take on diverse shapes, but in this case a semi-automatic tetrahedral grid was employed.

Because external aerodynamic simulations were performed, it has been necessary to develop an external domain. As presented in figure 3.1, two different domains were made, one for subsonic-flows and the second for supersonic-flows. That is because within the subsonic and transonic regimes, the domain's extent should encompass a sufficient width to prevent disruption of the flow field in all directions, while in supersonic conditions the required domain size can be smaller since shock-waves do not permit the propagation of perturbations upstream. The software used to generate the grid is *Ansys ICEM CFD* [47].

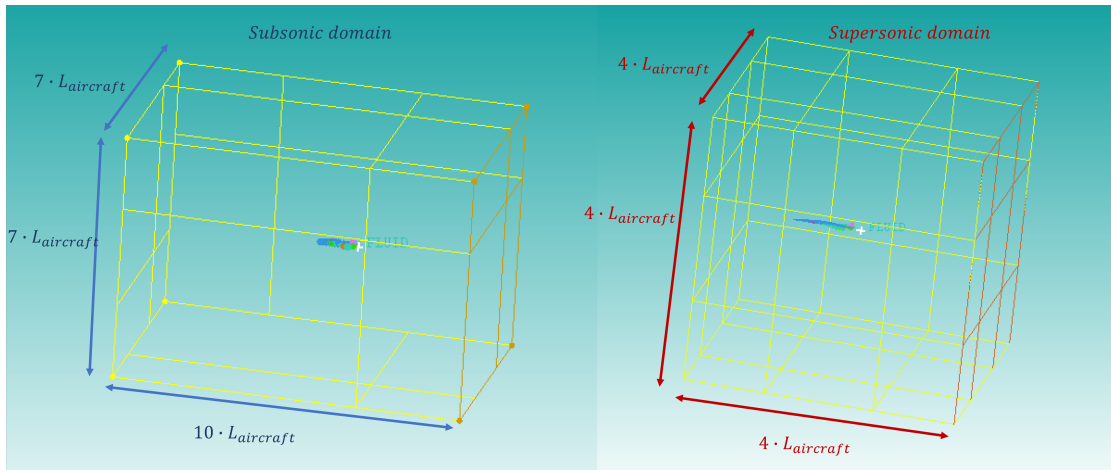


Figure 3.1: Subsonic and supersonic domains

Once the domains around the aircraft were created, it was necessary to define the different parts to be worked on later. In particular, the two parts called inlet and outlet were created on the domain so that the boundary conditions can later be applied; then, starting from the *CAD* model of the aircraft, eight different parts were created, grouping the main aircraft components: fuselage, canard, wing, horizontal tail, vertical tail, engine nacelle, engine inlet and outlet. These different parts on the aircraft were created in order to optimise the size of the grid elements

according to the surface to be meshed, so as not to risk building excessively small elements that would result in too high a computational load. As mentioned before, it should also be noted that since the chosen engine is a conceptual design whose study was carried out in parallel with this work, the engine inlet and outlet parts were created so that they could be, later on when defining the boundary conditions, considered as solid surfaces on which the aerodynamic coefficients studied were not integrated; a more correct approach would be to define, if the data are known, the engine input and output flow rates. Once the geometry was sorted out and checked that there were no holes between the connections of the various parts, the body object "fluid" was defined so as to allow *Fluent* to understand in which part of the domain between inlet and outlet there is air, and in which part the solid aircraft. It was then agreed on the most appropriate dimensions for the elements of each part, so as not to make too coarse a grid, nor too precise. Considering that *maximum size* determines the length of the edge segments on the surfaces, and *height ratio* determines the normal heights of the subsequent layers [48], table 3.1 summarises the choices made.

<i>Part</i>	<i>Maximum size [mm]</i>	<i>Height ratio</i>
Canard	100	1.1
Engine	100	1.1
Fuselage	250	1.1
Horizontal tail	100	1.1
Inlet	6000	1.1
Inlet engine	100	1.1
Outlet	6000	1.1
Outlet engine	100	1.1
Vertical tail	75	1.1
Wing	100	1.1

Table 3.1: Part mesh setup

After several attempts, two volumetric mesh with tetrahedral elements were created, obtaining about 5.2 million of elements for the subsonic grid and 2.8 for the supersonic one; lastly, the grids' quality, and the absence of errors that would later jeopardise the success of the fluid-dynamic simulations, were verified.

In the following figures are presented: the above and below views of the aircraft (Fig 3.2, 3.3, 3.4, 3.5), the two side views (Fig 3.6, 3.7, 3.8, 3.9), the front and back views (Fig 3.10, 3.11, 3.12, 3.13), an isometric view of the aircraft (Fig 3.14, 3.16), and a detail of the engine's nacelle (Fig 3.15, 3.17).

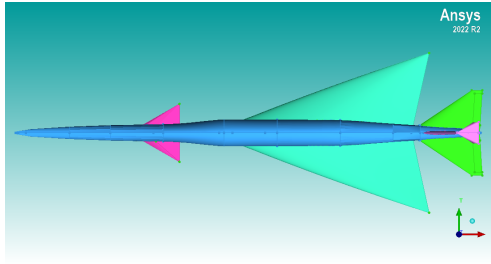


Figure 3.2: Above view of the aircraft - geometry

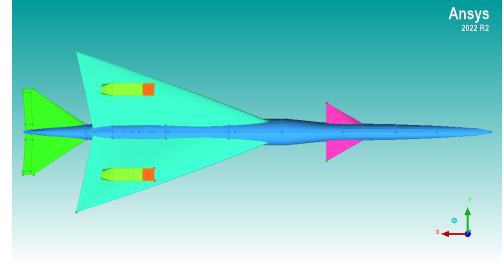


Figure 3.3: Below view of the aircraft - geometry

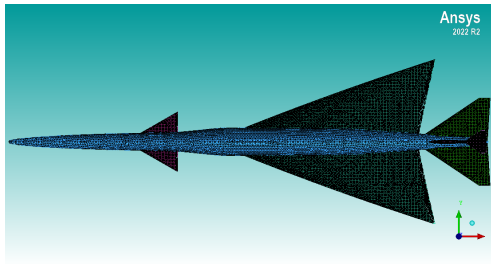


Figure 3.4: Above view of the aircraft - mesh

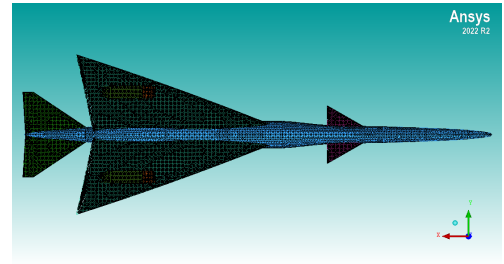


Figure 3.5: Below view of the aircraft - mesh

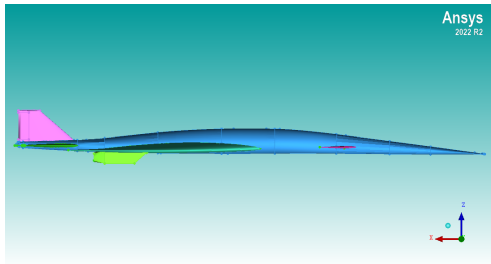


Figure 3.6: Right-side view of the aircraft - geometry

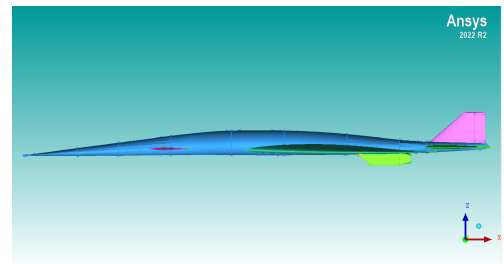


Figure 3.7: Left-side view of the aircraft - geometry

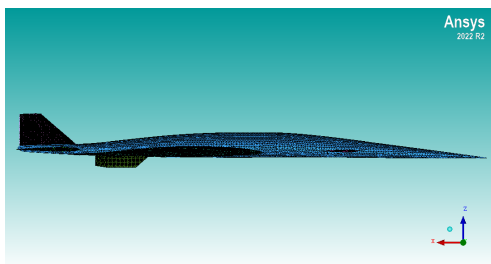


Figure 3.8: Right-side view of the aircraft - mesh

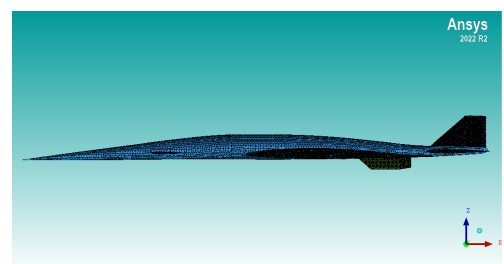


Figure 3.9: Left-side view of the aircraft - mesh

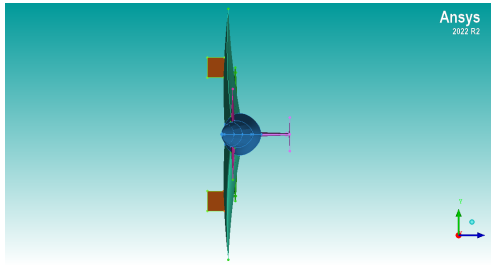


Figure 3.10: Front view of the aircraft - geometry

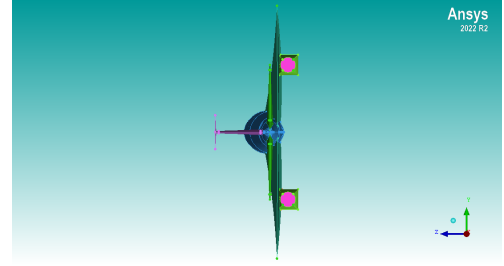


Figure 3.11: Rear view of the aircraft - geometry

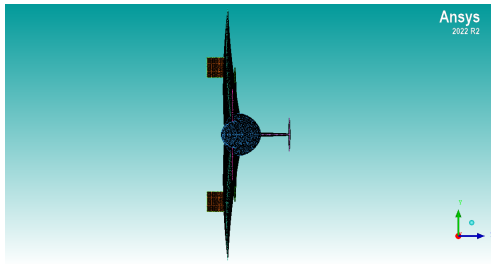


Figure 3.12: Front view of the aircraft - mesh

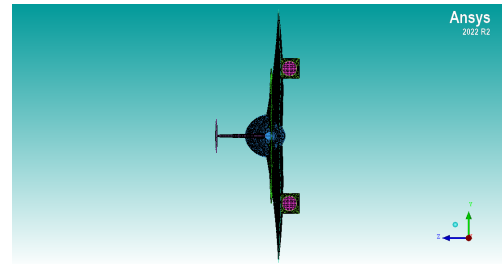


Figure 3.13: Rear view of the aircraft - mesh

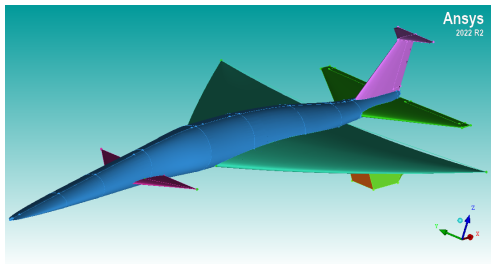


Figure 3.14: Isometric view of the aircraft - geometry

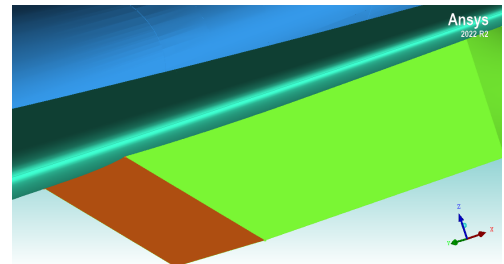


Figure 3.15: Detail of an engine's nacelle - geometry

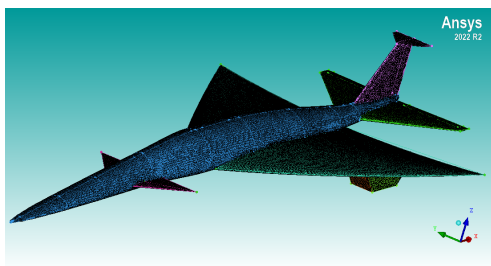


Figure 3.16: Isometric view of the aircraft - mesh

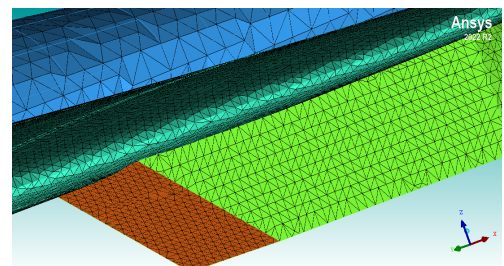


Figure 3.17: Detail of an engine's nacelle - mesh

Solution Method

Two different numerical solvers can be implemented in *Ansys Fluent* [45]:

- pressure-based;
- density-based.

Since, historically, the pressure-based solver was used for studies of low-speed flows, the density-based solver was chosen. It solves simultaneously the governing equations for mass, momentum, and energy. Given the nonlinear and coupled nature of these equations, multiple iterations of the solution-loop are necessary to achieve a convergence. The following steps take place during each iteration:

- Update the fluid properties using the current solution;
- Solve the governing equations;
- Verify the convergence of the equation set.

Within the density-based solution method, the process of linearizing the governing equations can either be "implicit" or "explicit" with regards to the dependent variables of interest. In any case, the governing equations are transformed into a linearized form, resulting in a set of equations for the dependent variables within each computational cell. This resulting linear system is then resolved to obtain an updated solution for the flow field. The implicit formulation is the one used for these simulations and is characterized by the fact that, when dealing with a specific variable, the unknown value within each cell is determined using a relationship that incorporates both known and unknown values from neighboring cells. Thus, each unknown quantity appears in multiple equations within the system, and the resolution of the equations needs to occur simultaneously to determine the unknown variables.

The spatial discretization method used is a first-order upwind scheme. In this method, the values at cell-faces are established assuming that cell-center values are the average for the entire cell. Since a value is maintained throughout the entire cell, the value at the face is equated to the cell-center value of the variable in the upstream cell. In order to construct a value at a face, the *Green-Gauss cell-based* gradient was used. This gradient is the simplest one and implies that the face value is equal to the arithmetic average of the values at the neighboring cell centers. The employed flow method is the *Advection Upstream Splitting Method - (AUSM)*, since it accurately and comprehensively handles flow across cell boundaries, considering thermo-kinematic variations of the fluid, and helping to achieve a more realistic solution.

Simulations setting

After generating and exporting the mesh grids with *Ansys ICEM CFD*, *Ansys Fluent 2022R2* was used as pre-processor for simulations setting, and later as solver, thanks to the computational power provided by HPC@POLITO (<http://hpc.polito.it>).

- Dimensions and options: 3D - double precision, since the geometry model is three-dimensional and there is a huge difference between the largest and smallest element size [49];
- Mesh scaling and displaying: since the model was created in *mm*, it was necessary to scale the dimensions to the International System of measurement, and display what has been loaded to verify the accuracy of the model on which simulations will be run (example in figure 3.18);

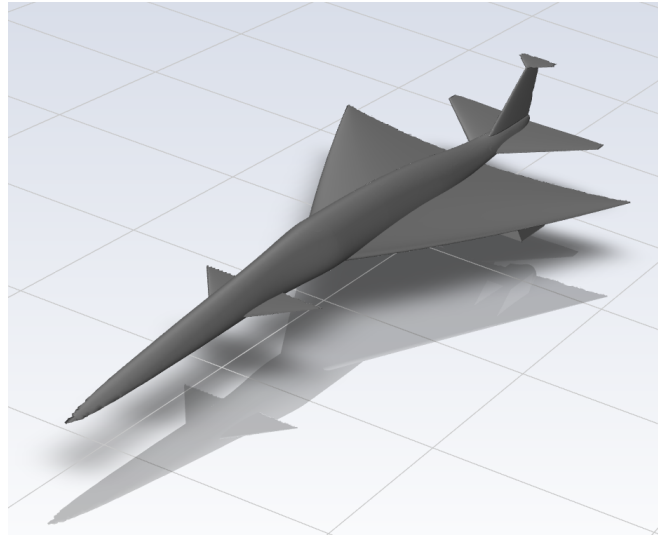


Figure 3.18: Overview of the imported model

- Solver type and time: density-based and steady;
- Energy equation activated and inviscid flow;
- Air as an ideal gas with constant $C_p = 1006.43 \text{ J}/(\text{kg K})$ and molecular weight $M_W = 28.966 \text{ kg}/\text{kmol}$;
- Boundary conditions:
 - Inlet type: pressure far field [49]. This condition allows the user to select the Mach number of the flow, the angle of attack as a composition of x,y, and z components, and the temperature of the flow

($T = 216.7 K @ 16000 m$ [50]). The Mach number and the angle of attack were varied for each simulation as will be presented below;

- Outlet type: pressure outlet [49]. This condition allows the user to select the temperature of the flow;
 - Engine inlet and outlet: solid walls.
- Reference values are the wing's surface $S = 112 m^2$ and the vehicle's length $L = 44 m$; the simulations must be computed from the inlet and the reference zone is *Fluid*;
 - Solution Method: Implicit formulation, *AUSM* flux type, Green-Gauss cell based and first order Upwind [49];
 - Solution Control: *Courant Number* = 1.2. This number represents the ratio of the numerical time step to the characteristic time scale in a simulation, and it is used to ensure stability and accuracy [43];
 - Report Definitions: the three force report requested (calculated on each aircraft surface except inlet and outlet engine) are C_X (force coefficient along the aircraft x-axis), C_Z (force coefficient along the aircraft z-axis) and C_{my} (moment coefficient around the aircraft y-axis). These outputs are the results for each simulation and will later be transformed into wind axes;
 - Monitors on residuals are turned off in order to speed up simulations;
 - Standard initialization before each simulation and number of iteration set at 10000 for each simulation.

Test Matrix

As stated at the beginning of this chapter, the aim of this section is to define a test-matrix to characterise the aircraft, and to be used as input for the mission simulation. A test matrix is a structured set of test cases used to evaluate the performance of the aircraft through *CFD* simulations. This matrix includes a range of problems with varying flow conditions, and its aim is to comprehensively assess the aerodynamic characteristics of the aircraft in terms of its lift, drag and moment coefficients.

The following test-matrix states that, for each Mach number, 6 different simulations are performed, with variable angle of attack from -5 to 20 degrees. As stated before, up to Mach 1.05, simulations are performed on the subsonic grid, while for Mach 1.20 and 1.50, simulations are performed on the supersonic grid. In each mesh, the aircraft is in a clean configuration, so the effects of the control surfaces are not being evaluated.

In table 4.1 the definition of the test matrix is presented.

Mach	AoA [deg]	Run [#]
0.30	$-5^\circ \rightarrow 20^\circ$, step 5°	6
0.60	$-5^\circ \rightarrow 20^\circ$, step 5°	6
0.80	$-5^\circ \rightarrow 20^\circ$, step 5°	6
0.95	$-5^\circ \rightarrow 20^\circ$, step 5°	6
1.05	$-5^\circ \rightarrow 20^\circ$, step 5°	6
1.20	$-5^\circ \rightarrow 20^\circ$, step 5°	6
1.50	$-5^\circ \rightarrow 20^\circ$, step 5°	6
Tot ->		42

Table 3.2: Test Matrix: definition

Once again, it is useful to repeat that the simulations are non-viscous, but when discussing the results, the engineering correction adopted will be presented.

3.2 Mission Simulation

ASTOS is an object-oriented software which has been specifically developed for trajectory simulation and optimization in aerospace applications [51]. It was primarily designed for space purposes such as simulating trajectories of launchers, satellites, and re-entry vehicles; nevertheless, with some considerations, it can also be applied to atmospheric flight scenarios, thus its application to the presented case study. *ASTOS* provides a Graphical User Interface that facilitates, on the one hand, problem formulations, such as the creation of the atmospheric environment in which the aircraft conducts the mission, and the definition of the vehicle specifications, such as its dimensions, mass properties, aerodynamic and propulsion characteristics; on the other hand, the Graphical User Interface allows the user to visualize the simulation's results, although in this case the results will be presented after elaboration in *Excel* environment for better clarity. As stated previously, the aim of this section is the mission simulation alone, aware of the fact that *ASTOS* allows to perform much more complex functions such as, for example, trajectory optimization and identification of optimum control parameters [52].

Critical inputs for trajectory simulation involve aerodynamic and propulsion databases. While the aerodynamic database was thoroughly detailed in the previous section, the fact that the aircraft is equipped with two state-of-the-art turbofan engines at a conceptual design stage caused a lack of data to assess a propulsion database. Therefore, thanks to the work of my colleague Francesco Piccionello, he managed to evaluate an algorithm to model this specific kind of engines [1]. Thanks to him, it was possible to evaluate a propulsion database, presented as a table where the net thrust, the specific fuel consumption, and the fuel mass flow are expressed as function of the Mach number and altitude.

Furthermore, to start the mission simulation, both the mass data of the aircraft, such as the Maximum Take-Off Weight and the Fuel Mass, respectively 39283 *kg* and 18434 *kg*, and other characteristic data gathered in table 3.3 have been inserted.

Input	Value	[]
Mach Number	1.5	
Planform Surface	243	m^2
Planform Surface (wing)	141.5	m^2
Wetted Surface	584.58	m^2
Wetted Surface (wing)	243.3	m^2
Exposed Wing Surface (planform - both sides)	112	m^2
Wing Span	14	m
Fuselage Length	44	m

Continued on next page

Input	Value	□
Fuselage Width	2.51	<i>m</i>
Mean Aerodynamic Chord of the Wing	13.12	<i>m</i>
Leading Edge Sweep Angle of the Wing	68	°
Wing Thickness Ratio (at MAC) - <i>NACA 64-206 airfoil</i>	6.00	%
Nacelle Length	6.5	<i>m</i>
Nacelle Diameter	1.6	<i>m</i>
Inlet Width	1.6	<i>m</i>
Horizontal Tail Thickness Ratio - <i>NACA 0006 airfoil</i>	6	%
Horizontal Tail Surface	22	<i>m</i> ²
Leading Edge Sweep Angle of the Horizontal Tail	54	°
Mean Aerodynamic Chord of the Horizontal Tail	6.04	<i>m</i>
Vertical Tail Thickness Ratio - <i>NACA 0006 airfoil</i>	6	%
Vertical Tail Wetted Surface (with rudder - both sides)	25	<i>m</i> ²
Leading Edge Sweep Angle of the Vertical Tail	41	°
Mean Aerodynamic Chord of the Vertical Tail	4.06	<i>m</i>
Canard Thickness Ratio - <i>GOE 443 airfoil</i>	5	%
Canard Wetted Surface (both sides)	14	<i>m</i> ²
Leading Edge Sweep Angle of the Canard	60	°
Mean Aerodynamic Chord of the Canard	2.36	<i>m</i>

Table 3.3: Other input data for *ASTOS*

Once this has been done, it was possible to generate the various phases of the mission:

- Take-off;
- Subsonic climb;
- Supersonic climb;
- Supersonic cruise;
- Supersonic descent;
- Subsonic descent;
- Landing.

Within each of these phases, a series of numerical values were entered relating to the angle of attack and the throttle; by adjusting these parameters, it was possible to bring the aircraft to follow the desired trajectory.

3.3 CO_2 Metric Value

3.3.1 CO_2 emissions evaluation metric value

The CO_2 emissions evaluation metric value [kg/km] [42] is a quantitative measurement used to assess the environmental impact of an activity in terms of its carbon dioxide emissions, and it is designed to provide a standardised way of comparing and evaluating the carbon emissions associated with different scenarios. It serves as a valuable tool for both industries and governments so as to reduce the carbon footprint and mitigate the impacts of climate change, since it enables informed choices and policy formulation.

The formula for calculating the CO_2 metric value incorporates the Specific Air Range - SAR , and the Reference Geometric Factor - RGF as presented below, and it is a SAR -based metric adjusted to take into account fuselage size with the RGF :

$$CO_2 MV = \frac{1}{\frac{(SAR)_{avg}}{(RGF)^{0.24}}} \quad (3.33)$$

As stated in ICAO Annex 16 Vol III [42], the value of the CO_2 emissions evaluation metric must not exceed the value specified in the graph 3.19:

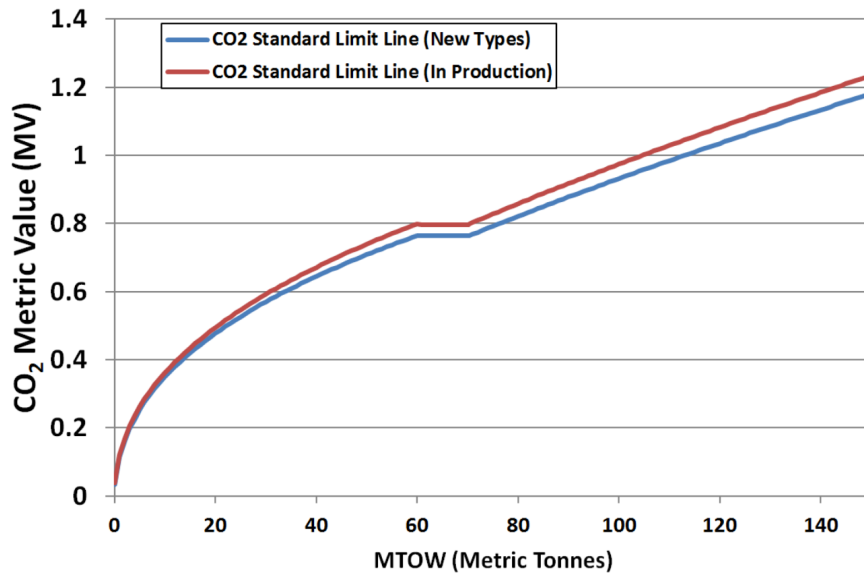


Figure 3.19: The CO_2 Standard Regulatory Limits (Source: [53])

3.3.2 Specific Air Range - *SAR*

Specific Air Range is a metric used to measure the fuel efficiency of an aircraft; it quantifies how far an aircraft can travel per unit of fuel consumed as follows:

$$SAR = \frac{\textit{kilometre range}}{\textit{unit of kg fuel}} \quad (3.34)$$

Equation 3.33 is based on the average *SAR* because *ICAO Annex 16 Volume III* states that, in order to be tested in accordance to the standard, the ratio $1/SAR$ must be evaluated for each of the following three reference mass points, function of the Maximum Take-Off Mass *MTOM* in $[kg]$:

- *High gross mass* = $0.92 \cdot MTOM$
- *Low gross mass* = $(0.45 \cdot MTOM) + (0.63 \cdot MTOM^{0.924})$
- *Mid gross mass* = $\frac{\textit{High gross mass} + \textit{Low gross mass}}{2}$

As presented above, to assess the fuel efficiency of an aircraft, the CO_2 metric system employs three different test points that mirror fuel consumption patterns during the cruising phase; for subsonic aircrafts, these three reference points are representative of the beginning, end and mid-cruise conditions respectively, as presented in figure 3.20:

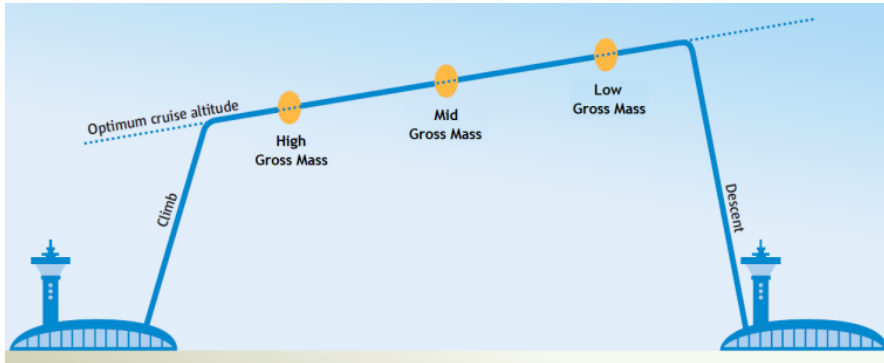


Figure 3.20: Subsonic cruise reference points (Source: [54])

In addition, in order to be compliant with the regulation, the following (among others [42]) reference conditions for determining the specific air range must be adopted:

- Altitude and airspeed selected by the applicant;
- Steady, straight and level flight;

- Longitudinal and lateral trim;
- Standard day atmosphere [50];
- Fuel lower heating value of 43.217 MJ/kg

To therefore assess the SAR_{avg} in a manner compliant with the regulation [42], the ratio between the true velocity [km/s] over the total fuel mass flow [kg/s] must be calculated for each of the three reference mass points; then, the arithmetic average of the three SAR values must be computed. It was therefore the need to make these calculations that led to performing a mission simulation, so that certain aircraft quantities such as the true velocity and the fuel flow rate could be known at any given time.

However, as recommended by *EASA* [54] and verified later in chapter 4, the definition of the reference mass points used for subsonic aircrafts is not suitable for supersonic airplanes, due to their higher fuel fraction compared to subsonic designs. Hence, both the defined high gross mass point and low gross mass point do not accurately represent the aircraft's weight at the start and end of a cruise segment; in particular, it is specifically the low mass point that is largely overestimated when performing the assessment for a supersonic aircraft, following the existing regulations. To address this problem, various solutions were explored using performance models of conceptual *SST* airplanes, and it was finally decided, in line with [54], that the airplane's applicant should choose high and low gross masses that represent the initial-cruise and end-of-cruise conditions, so as to keep valid the idea of the subsonic regulation, but adapting it for a supersonic case study.

3.3.3 Reference Geometric Factor - RGF

The Reference Geometric Factor - RGF is a dimensionless parameter used to adjust the average reciprocal of the Specific Air Range discussed earlier; it is determined by measuring the aircraft's fuselage size and normalizing it to an area of 1 m^2 in order to make it dimensionless [42].

In this case of a single deck configuration, the RGF must be calculated by determining the area enclosed by the outermost contour of the fuselage, and projecting it onto a flat plane that is parallel to the main deck floor, so as to effectively capture the maximum width of the fuselage; this value must then be normalized with 1 m^2 . The RGF covers all pressurized spaces on the main deck, including aisles, auxiliary spaces, passageways, and cargo area, but do not cover integral fuel tanks within the cabin, unpressurized fairings, and crew rest or work areas. Furthermore, the cockpit crew zone is not considered in the RGF assessment and the aft boundary is the pressurized bulkhead.

It is important be advised that the area of concern of *RGF* may not be aligned with the cabin floor space, as it relies on the widest section of the fuselage outer mold line, which might vary across the airplane's length. In order to be able to assess the *RGF*, the following information must be known:

- Longitudinal view of the aircraft with main dimensions;
- Length of the cabin;
- Maximum fuselage width and actual floor width at start and end position of the cabin.

In figures 3.21 and 3.22 the conditions explained above are represented graphically.

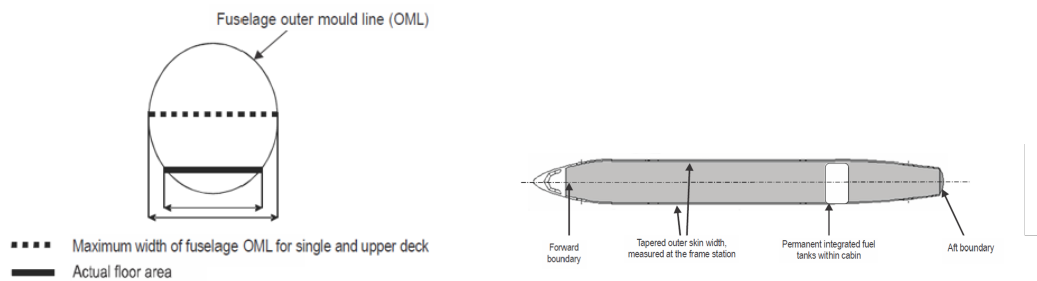


Figure 3.21: *RGF* cross sectional and longitudinal views (Source: [42])

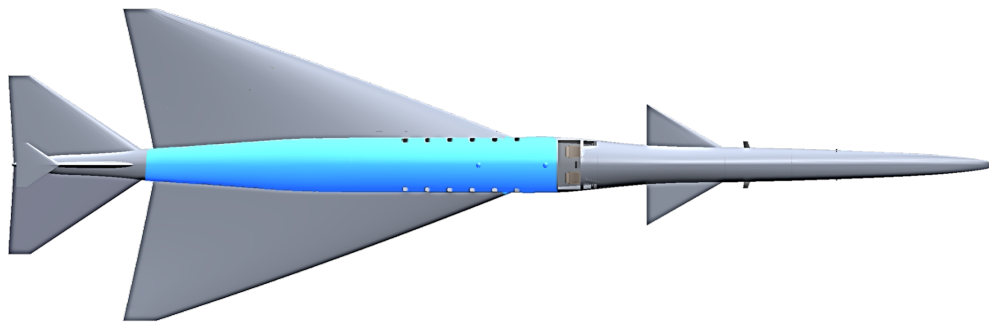


Figure 3.22: *RGF* plan view

Chapter 4

Results

4.1 Aerodynamic results

In this section, the focus is on the outcomes extracted from the computational fluid dynamic simulations. In table 4.1 an overview of the test matrix is presented while in table 4.2 each case is detailed with results.

Mach	AoA [deg]	Run [#]
0.30	-5° -> 20°, step 5°	6
0.60	-5° -> 20°, step 5°	6
0.80	-5° -> 20°, step 5°	6
0.95	-5° -> 20°, step 5°	6
1.05	-5° -> 20°, step 5°	6
1.20	-5° -> 20°, step 5°	6
1.50	-5° -> 20°, step 5°	6
Tot ->		42

Table 4.1: Test Matrix: definition

As can be seen from table 4.1, for each selected Mach number, the angle of attack was shifted from -5 to 20 degrees, for a total of 6 simulations per Mach number, thus 42 simulations in total.

GRID	Mach	Alpha	C_{my}	C_z	C_x
SUBSONIC	0.30	-5	0.14428	-0.21774	0.011011

continued on next page

GRID	Mach	Alpha	Cmy	Cz	Cx
SUBSONIC	0.30	0	-0.02517	0.037867	0.013672
SUBSONIC	0.30	5	-0.18901	0.28652	0.0041259
SUBSONIC	0.30	10	-0.35728	0.54552	-0.0043639
SUBSONIC	0.30	15	-0.5468	0.83581	-0.016902
SUBSONIC	0.30	20	-0.76139	1.1612	-0.029251
SUBSONIC	0.60	-5	0.084221	-0.12643	0.0068476
SUBSONIC	0.60	0	-0.015017	0.022617	0.0083183
SUBSONIC	0.60	5	-0.19947	0.26716	0.0065512
SUBSONIC	0.60	10	-0.36452	0.59332	-0.00461
SUBSONIC	0.60	15	-0.5695	0.8667	-0.01154
SUBSONIC	0.60	20	-0.82162	1.1872	-0.012567
SUBSONIC	0.80	-5	0.15694	-0.23304	0.014092
SUBSONIC	0.80	0	-0.029017	0.04381	0.016108
SUBSONIC	0.80	5	-0.20578	0.31005	0.0096577
SUBSONIC	0.80	10	-0.38393	0.58412	-0.00017605
SUBSONIC	0.80	15	-0.59113	0.89941	-0.0073776
SUBSONIC	0.80	20	-0.82162	1.2472	-0.012567
SUBSONIC	0.95	-5	0.16857	-0.24672	0.019962
SUBSONIC	0.95	0	-0.032363	0.048863	0.022298
SUBSONIC	0.95	5	-0.2296	0.34094	0.016872
SUBSONIC	0.95	10	-0.42519	0.6375	0.010149
SUBSONIC	0.95	15	-0.64048	0.96228	0.0067304
SUBSONIC	0.95	20	-0.88383	1.3417	0.0065006
SUBSONIC	1.05	-5	0.21235	-0.30461	0.034971
SUBSONIC	1.05	0	-0.041362	0.062506	0.034044
SUBSONIC	1.05	5	-0.24424	0.36956	0.03061
SUBSONIC	1.05	10	-0.47018	0.66421	0.02463
SUBSONIC	1.05	15	-0.6578	0.95678	0.0061001
SUBSONIC	1.05	20	-0.85613	1.3301	0.01991
SUPERSONIC	1.20	-5	0.17774	-0.24899	0.024372
SUPERSONIC	1.20	0	-0.018071	0.028743	0.017896
SUPERSONIC	1.20	5	-0.23049	0.33522	0.024532
SUPERSONIC	1.20	10	-0.4342	0.63392	0.017505
SUPERSONIC	1.20	15	-0.64304	0.90327	0.011868
SUPERSONIC	1.20	20	-0.86768	1.2709	0.01009
SUPERSONIC	1.50	-5	0.16192	-0.22683	0.021802

continued on next page

GRID	Mach	Alpha	Cmy	Cz	Cx
SUPERSONIC	1.50	0	-0.016098	0.027771	0.02466
SUPERSONIC	1.50	5	-0.19717	0.28603	0.021175
SUPERSONIC	1.50	10	-0.3939	0.56827	0.015499
SUPERSONIC	1.50	15	-0.59411	0.85951	0.010645
SUPERSONIC	1.50	20	-0.79557	1.1539	0.0075088

Table 4.2: Test Matrix: results

In order to transform the aerodynamic coefficients from body axes into wind-axes, the following equations for the lift coefficient and drag coefficient were used:

$$C_L = C_z \cos(\alpha) - C_x \sin(\alpha) \quad (4.1)$$

$$C_D = C_z \sin(\alpha) + C_x \cos(\alpha) \quad (4.2)$$

Furthermore, in table 4.2 the moment coefficients are calculate with reference to the aircraft's bow, while for stability evaluations, it is important to transport these values to the center of gravity. This operation is possible applying equation 4.3, and keeping in mind that the aircraft's center of gravity is positioned at $x_{cg} = 22.56 m$ from the bow, and the reference length is the aircraft's length $l_{ref} = 44 m$:

$$C_{my_{cg}} = C_{my} + C_z \frac{x_{cg}}{l_{ref}} \quad (4.3)$$

With these considerations in mind, the results presented in table 4.3 can be derived:

GRID	Mach	Alpha	Cl	Cd	Cm_cg
SUB	0.30	-5	-0.215951762	0.029946391	0.103922682
SUB	0.30	0	0.037867	0.013672	0.000766655
SUB	0.30	5	0.285070109	0.029082063	-0.067828519
SUB	0.30	10	0.537990109	0.090430951	-0.092756249
SUB	0.30	15	0.811705024	0.199997468	-0.080361805
SUB	0.30	20	1.101175502	0.369666842	-0.020718577
SUB	0.60	-5	-0.125352088	0.017840643	0.061023047
SUB	0.60	0	0.022617	0.0083183	0.000618675
SUB	0.60	5	0.265572401	0.029810799	-0.07246291

Continued on next page

GRID	Mach	Alpha	Cl	Cd	Cm_cg
SUB	0.60	10	0.585106654	0.098488973	-0.088410372
SUB	0.60	15	0.840154685	0.213171682	-0.078826499
SUB	0.60	20	1.119901247	0.394237197	-0.027029785
SUB	0.80	-5	-0.230925014	0.03434915	0.114816568
SUB	0.80	0	0.04381	0.016108	0.001230193
SUB	0.80	5	0.308028442	0.036643588	-0.068865431
SUB	0.80	10	0.575276475	0.101257998	-0.095593384
SUB	0.80	15	0.870672811	0.225658223	-0.07743025
SUB	0.80	20	1.176282804	0.414758406	-0.006508576
SUB	0.95	-5	-0.244041353	0.041389103	0.12781954
SUB	0.95	0	0.048863	0.022298	0.005704607
SUB	0.95	5	0.338172129	0.046522676	-0.071199506
SUB	0.95	10	0.626052587	0.120695527	-0.097310982
SUB	0.95	15	0.927749148	0.255557458	-0.072834106
SUB	0.95	20	1.258562253	0.464996992	0.011833247
SUB	1.05	-5	-0.300402944	0.061386436	0.170264072
SUB	1.05	0	0.062506	0.034044	0.012836575
SUB	1.05	5	0.365485875	0.062702796	-0.062525713
SUB	1.05	10	0.649842203	0.139594671	-0.101479438
SUB	1.05	15	0.92259969	0.25352513	-0.08374687
SUB	1.05	20	1.243075534	0.473630273	0.034669073
SUP	1.20	-5	-0.245918358	0.045980166	0.137112311
SUP	1.20	0	0.028743	0.017896	0.008630505
SUP	1.20	5	0.331806282	0.053654996	-0.064523513
SUP	1.20	10	0.621249619	0.127318113	-0.095308069
SUP	1.20	15	0.869420157	0.245247087	-0.084457059
SUP	1.20	20	1.190804369	0.444154899	-0.000728301
SUP	1.50	-5	-0.224066674	0.041488574	0.124509374
SUP	1.50	0	0.027771	0.02466	0.016406116
SUP	1.50	5	0.283096047	0.04602358	-0.055070857
SUP	1.50	10	0.556945329	0.113942585	-0.088020687
SUP	1.50	15	0.827467778	0.232739838	-0.071876562
SUP	1.50	20	1.081743154	0.401713007	-0.006197429

Table 4.3: Test Matrix: updated results

Before proceeding by presenting the charts obtainable from these data, it is

important to remember that the simulations were based on inviscid equations. In order to take into account the viscous effect, so as to later perform a more realistic mission simulation, it is possible to use the following correction equation [55]:

$$\Delta C_{d_{\text{viscous corrected}}} = \alpha \cdot \frac{1}{[\text{Log}(Re)]^{2.58}} \cdot \frac{1}{(1 + \beta M^2)^\gamma} \cdot \frac{A_{wet}}{A_{ref}} \quad (4.4)$$

Where:

α is a parameter depending on the vehicle configuration,

$\frac{1}{[\text{Log}(Re)]^{2.58}}$ represents the turbulent flat plate theory,

$\frac{1}{(1 + \beta M^2)^\gamma}$ represents the compressibility effects,

$\frac{A_{wet}}{A_{ref}}$ represents the wetted over reference area ratio.

(4.5)

Even if specifically studied for waverider configurations, the previous equation still provides acceptable results; from [55]: $\alpha = 0.455$, $\beta = 0.144$, and $\gamma = 0.65$, while, for this configuration, $A_{wet} = 584.58 \text{ m}^2$ and $A_{ref} = 141.5 \text{ m}^2$.

In figure 4.1 how the lift coefficient changes with reference to the angle of attack is illustrated. The $Cl - \alpha$ curves are parameterized with the Mach number and always show a linear increasing trend as expected. It is noteworthy the fact that the aircraft does not stall even for transonic Mach numbers at $\alpha = 20^\circ \text{ deg}$.

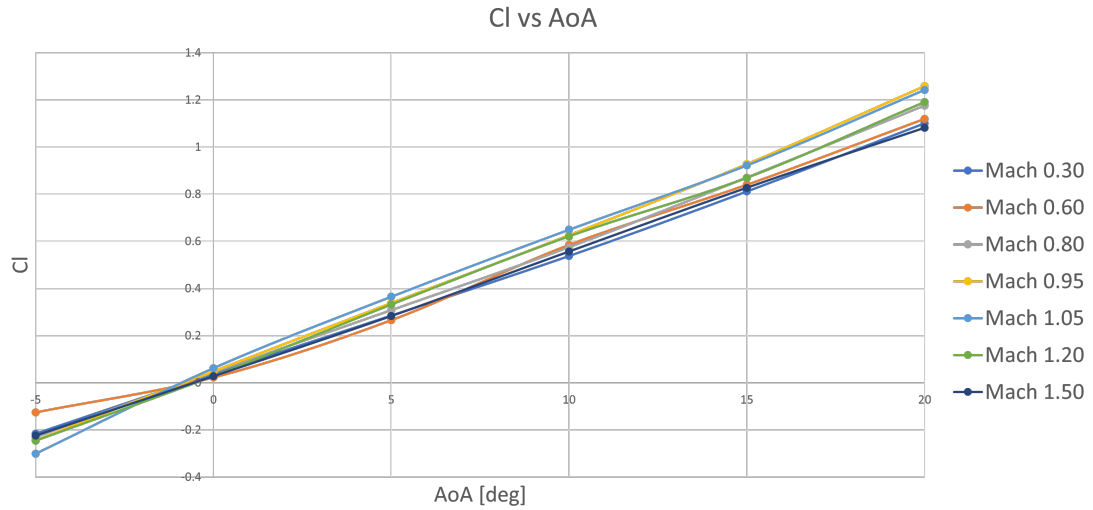


Figure 4.1: Cl vs α

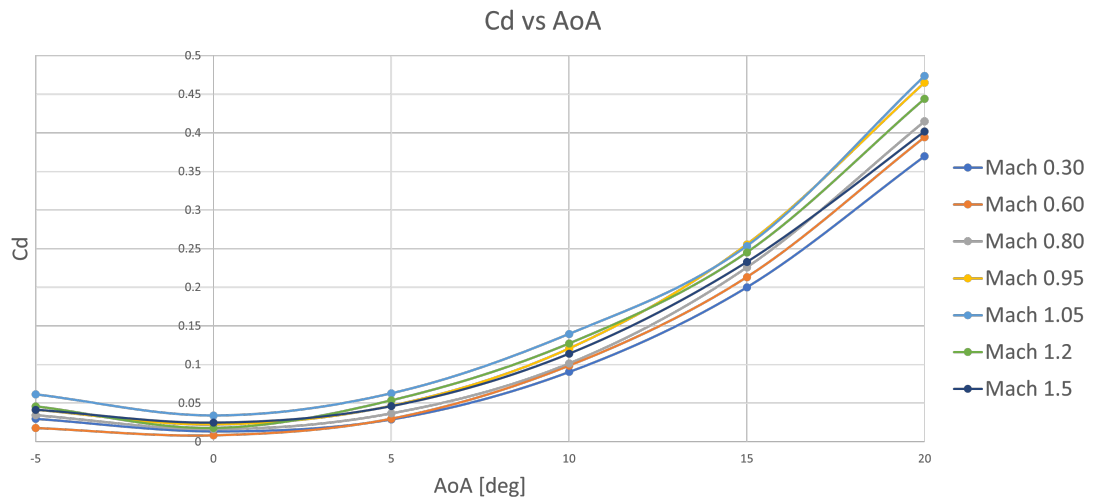


Figure 4.2: Cd vs α

In figure 4.2 how the inviscid drag coefficient changes with reference to the angle of attack is presented. The $Cd - \alpha$ curves are parameterized with the Mach number

and always show an increasing trend as expected; in addition, as one could imagine, the highest values of Cd , at a fixed angle of attack, are recorded in the transonic regime.

By doing the ratio Cl/Cd it is possible to compute the lift to drag ratio of the aircraft, presented in figure 4.3:

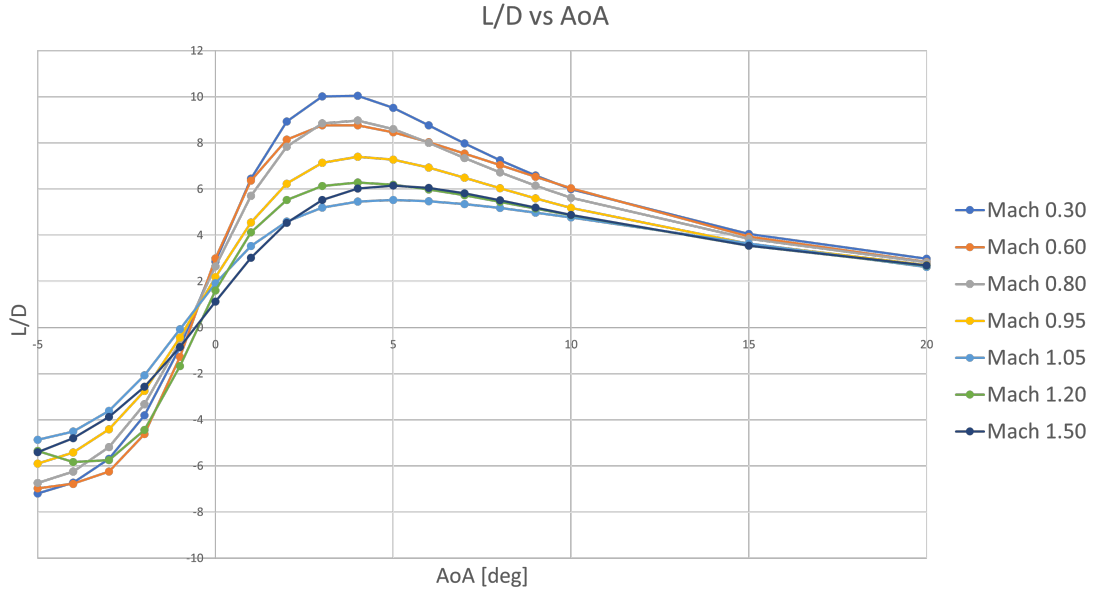


Figure 4.3: L/D vs α

Applying the equation 4.4 it is possible to correct the inviscid values, obtaining Cd_{visc} and the viscous corrected lift to drag ratio:

Mach	Alpha	Cd	L/D	Cd_vis	L/D_vis
0.30	-5	0.029946391	-7.211278311	0.040191865	-5.373021605
0.30	0	0.013672	2.769675249	0.023917474	1.583235738
0.30	5	0.029082063	9.802265674	0.039327537	7.248613264
0.30	10	0.090430951	5.949181124	0.100676426	5.343754564
0.30	15	0.199997468	4.058576508	0.210242942	3.860795595
0.30	20	0.369666842	2.978832231	0.379912316	2.898499092
0.60	-5	0.017840643	-7.026208944	0.027101453	-4.625290228
0.60	0	0.0083183	2.718944977	0.01757911	1.286583897
0.60	5	0.029810799	8.90859723	0.039071609	6.79706844

Continued on next page

Mach	Alpha	Cd	L/D	Cd_visc	L/D_visc
0.60	10	0.098488973	5.940834147	0.107749783	5.430235096
0.60	15	0.213171682	3.941211497	0.222432492	3.77712211
0.60	20	0.394237197	2.840678797	0.403498007	2.775481481
0.80	-5	0.03434915	-6.722874187	0.043239703	-5.340578207
0.80	0	0.016108	2.719766576	0.024998553	1.752501457
0.80	5	0.036643588	8.406066723	0.04553414	6.764780017
0.80	10	0.101257998	5.68129418	0.110148551	5.222733038
0.80	15	0.225658223	3.858369526	0.234548776	3.712118336
0.80	20	0.414758406	2.836067426	0.423648958	2.776550681
0.95	-5	0.041389103	-5.896270584	0.050068221	-4.87417667
0.95	0	0.022298	2.191362454	0.030977117	1.577390163
0.95	5	0.046522676	7.268974157	0.055201793	6.126107679
0.95	10	0.120695527	5.187040498	0.129374644	4.839067115
0.95	15	0.255557458	3.630295731	0.264236575	3.511055
0.95	20	0.464996992	2.706602998	0.473676109	2.657010198
1.05	-5	0.061386436	-4.89363718	0.06994562	-4.294807086
1.05	0	0.034044	1.836035718	0.042603184	1.46716733
1.05	5	0.062702796	5.828860891	0.07126198	5.128763954
1.05	10	0.139594671	4.655207811	0.148153855	4.386265899
1.05	15	0.25352513	3.639085757	0.262084314	3.520240013
1.05	20	0.473630273	2.624569428	0.482189457	2.577981571
1.20	-5	0.045980166	-5.348357386	0.054382887	-4.521980548
1.20	0	0.017896	1.606113098	0.026298722	1.092942858
1.20	5	0.053654996	6.184070528	0.062057718	5.346736754
1.20	10	0.127318113	4.879506986	0.135720834	4.577407908
1.20	15	0.245247087	3.54507843	0.253649808	3.427639716
1.20	20	0.444154899	2.681056478	0.45255762	2.631276803
1.50	-5	0.041488574	-5.400683914	0.049638564	-4.513963668
1.50	0	0.02466	1.126155718	0.03280999	0.846419034
1.50	5	0.04602358	6.151108794	0.05417357	5.225722577
1.50	10	0.113942585	4.887947095	0.122092575	4.561664193
1.50	15	0.232739838	3.555333654	0.240889828	3.435046576
1.50	20	0.401713007	2.69282581	0.409862997	2.639279861

Table 4.4: Test Matrix: viscous results

In figure 4.4 is presented a comparison between Cd and Cd_{visc} , with reference

to the angle of attack, for $M = 0.30$ and $M = 1.05$ as examples. It is possible to note that, as one could imagine, $Cd_{visc} > Cd$.

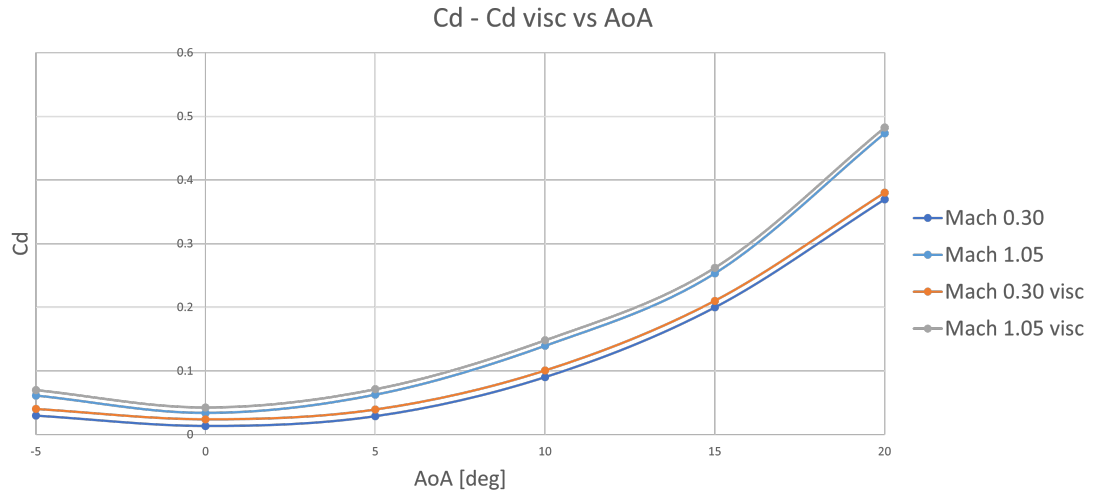


Figure 4.4: Cd vs Cd_{visc}

In figure 4.5 is presented a comparison between L/D and L/D_{visc} , with reference to the angle of attack, for $M = 0.30$ and $M = 1.05$ as examples. It is possible to note that, as one could imagine, $L/D_{visc} < L/D$.

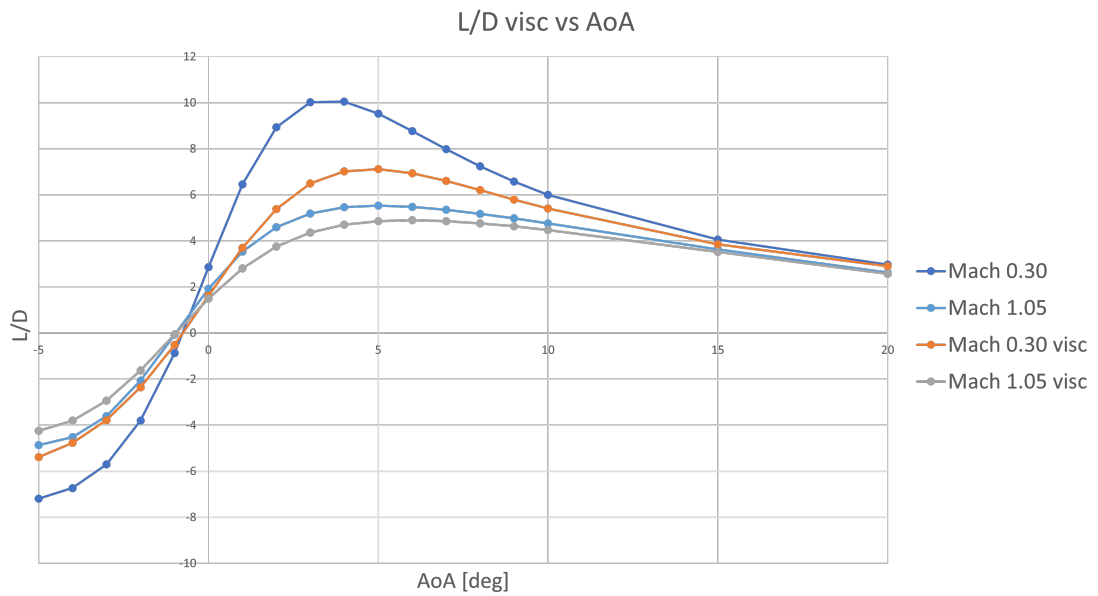


Figure 4.5: L/D vs L/D_{visc}

In figure 4.6 the inviscid drag polar is presented, that is how the drag coefficient changes with reference to lift coefficient. The $Cd - \alpha$ curves are parameterized with the Mach number and show a quasi-parabolic trend as expected.

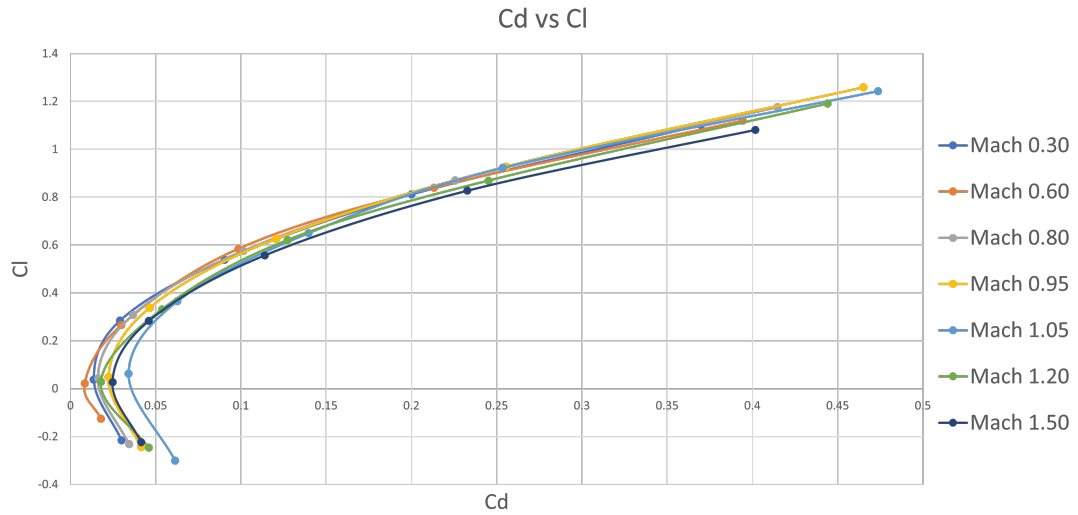


Figure 4.6: Cd vs Cl

Considering viscosity, the curves shift right towards an increase in the drag coefficient as shown in figure 4.7 for $M = 0.3$ and $M = 1.05$.

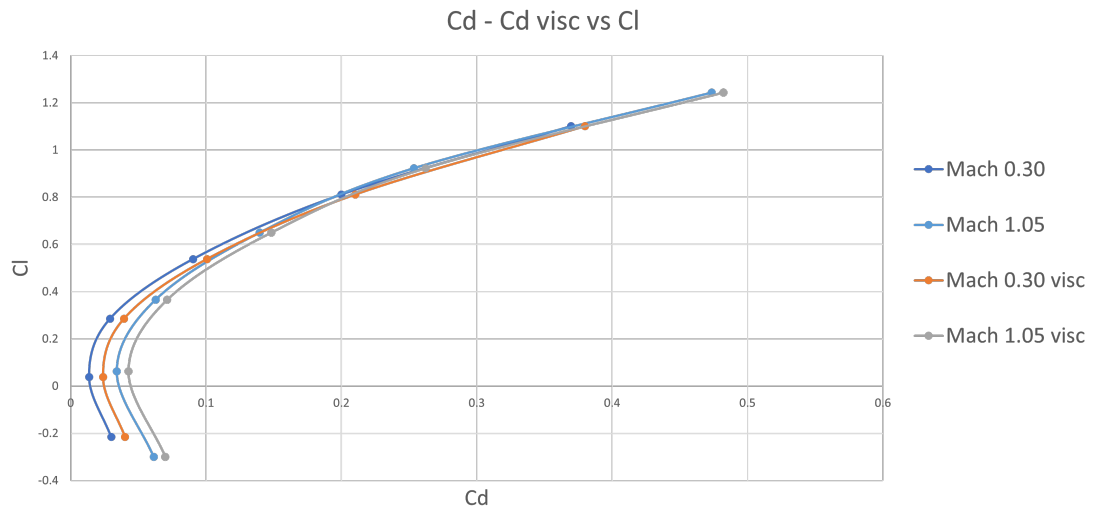


Figure 4.7: Cd vs Cd_{visc}

In conclusion, in figures 4.8 and 4.9 are presented the variation of the moment coefficient, calculated respectively at the front of the aircraft and in the center of gravity, with reference to the angle of attack.

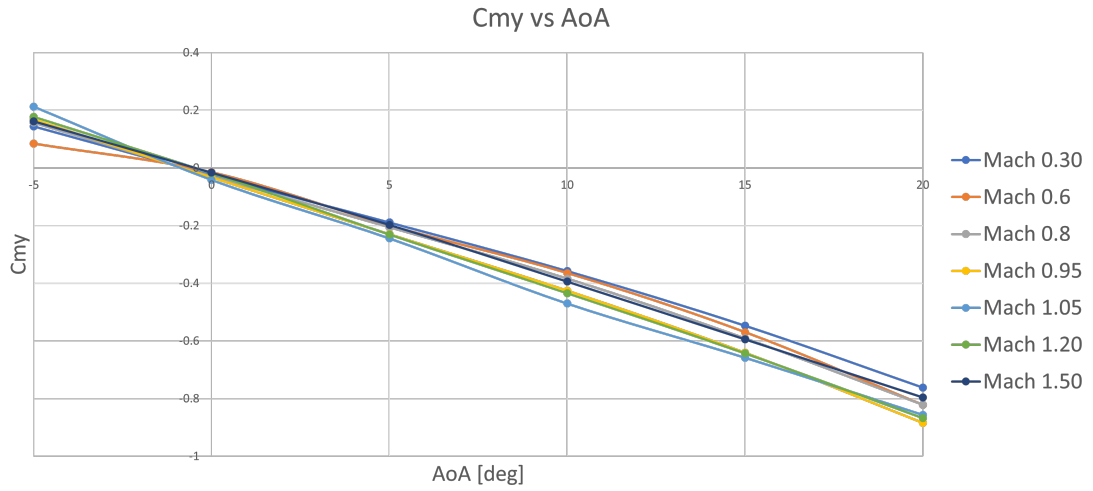


Figure 4.8: C_m vs α

Keeping in mind that $L_{ref} = 44\text{ m}$ and $x_{cg} = 22.56\text{ m}$, figure 4.9 is obtained using:

$$C_{m_{y_{cg}}} = C_{m_y} + C_z \frac{x_{cg}}{l_{ref}} \quad (4.6)$$

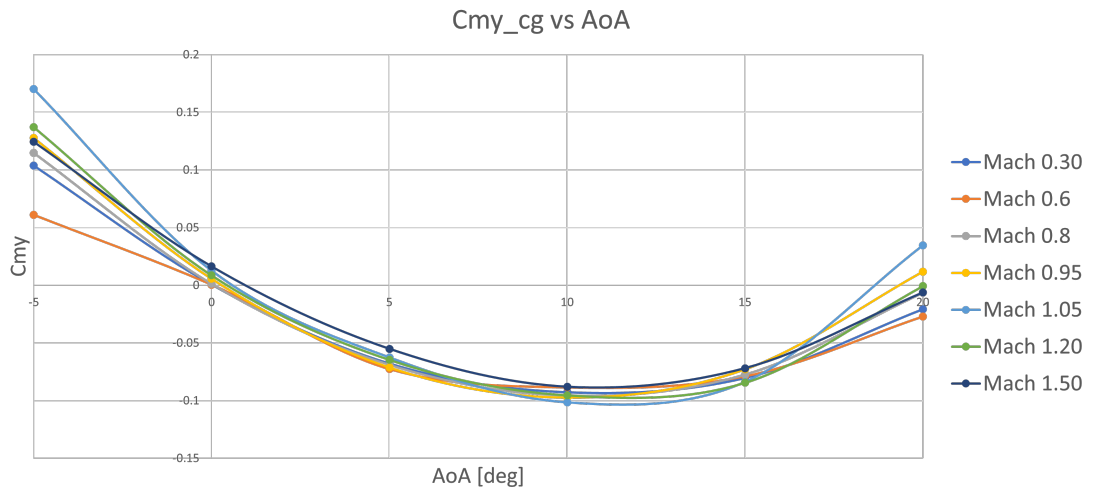


Figure 4.9: $C_{m_{y_{cg}}}$ vs α

4.2 Mission simulation results

In this section, the focus shifts to the results of the mission simulation, presenting the aircraft's performance during the mission.

The first pivotal insight emerges from figure 4.10, where it is shown that the aircraft successfully performs a supersonic cruise at *Mach* 1.5 at an altitude of approximately 16 *km*.

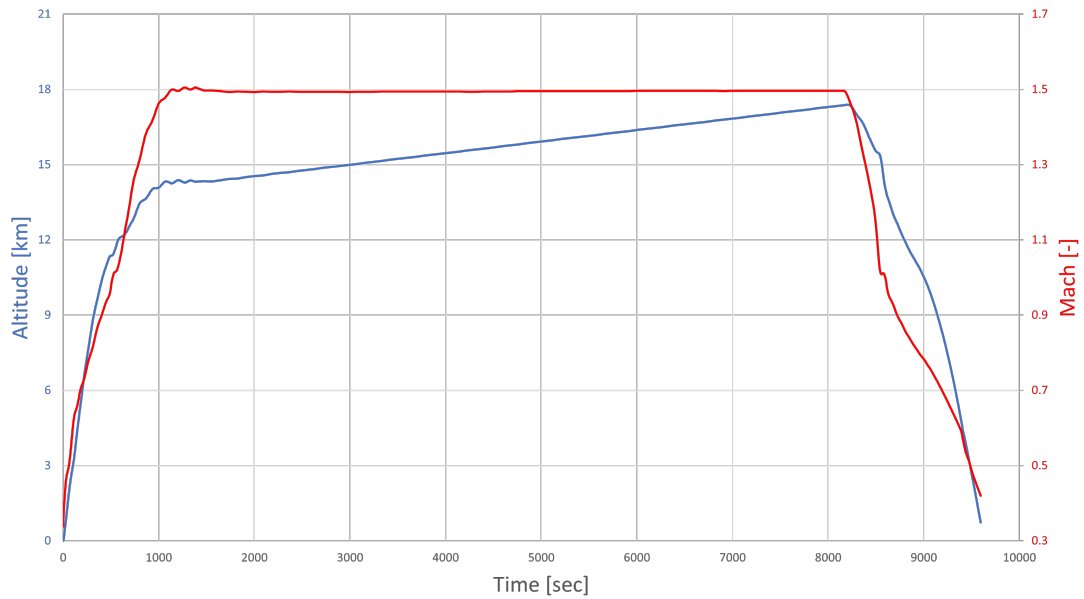


Figure 4.10: Altitude and Mach performances

The graph of figure 4.11 captures the evolution of both the total aircraft mass and propellant mass, presenting the equilibrium between fuel consumption and the consequential reduction in overall mass.

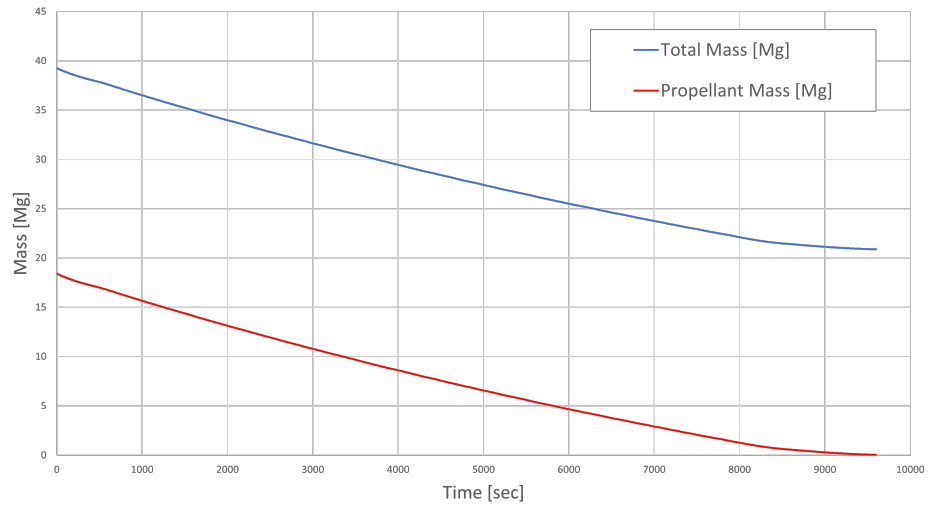


Figure 4.11: Total and propellant mass performances

In figure 4.12, it is possible to see that the angle of attack starts at 10 deg during the initial ascent, and converges to a steady value of around 2.3 deg during the cruise phase.

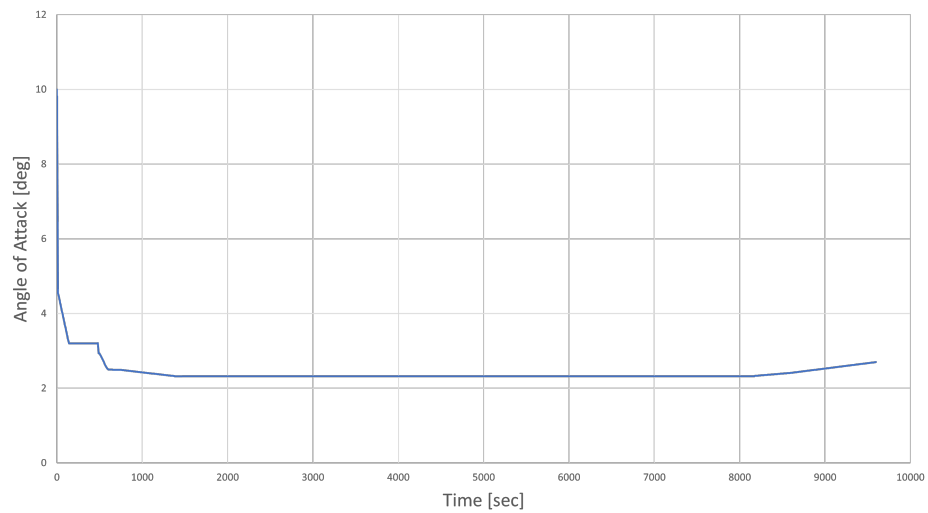


Figure 4.12: Angle of attack performance

In figure 4.13 is presented a graphical representation of the aircraft's lift to drag ratio and, although the cruise phase demonstrates an L/D below 4, it is important to acknowledge the preliminary nature of the configuration, urging further refinement and optimization.

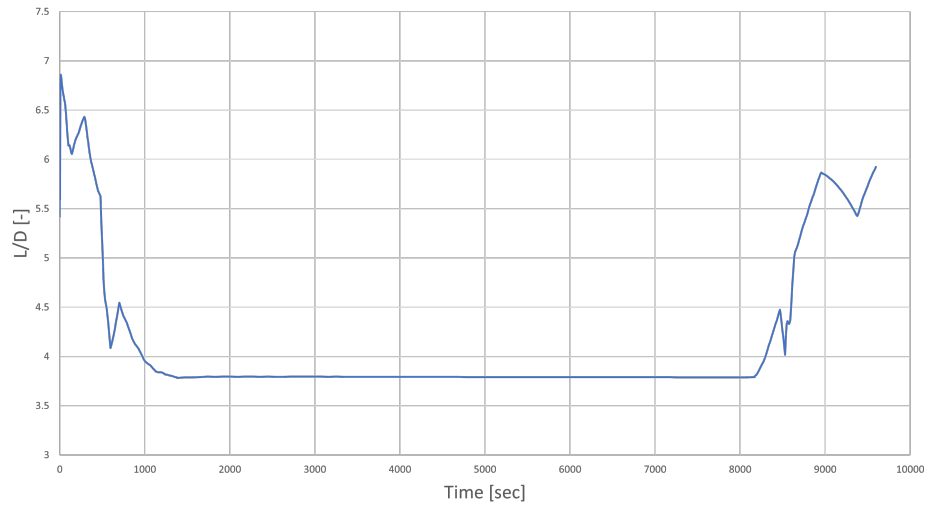


Figure 4.13: Efficiency performance

In figure 4.14, the engines ability to create thrust while effectively counteracting aerodynamic drag is presented.

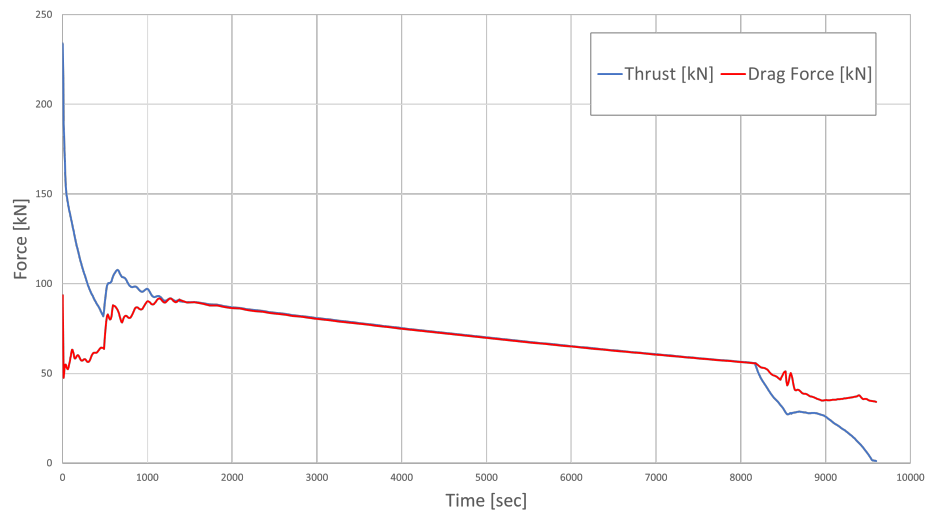


Figure 4.14: Thrust and drag performances

Lastly, in figure 4.15 the aircraft's capability to cover a distance greater than the required 3500 km is demonstrated.

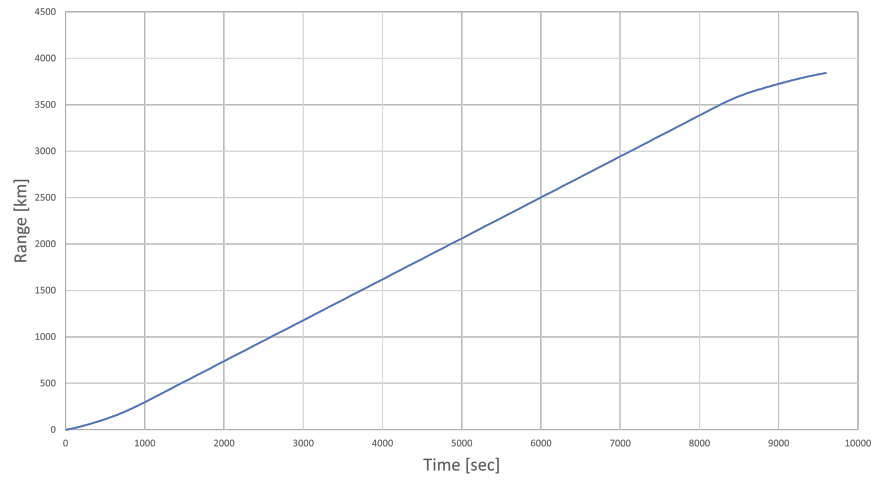


Figure 4.15: Range performance

4.3 CO_2 Metric Value results

After characterising the aircraft's aerodynamic performance through *CFD* simulations, and simulating a standard mission for supersonic business jets, it was finally possible to assess the airplane's CO_2 impact.

With reference to the regulations discussed in section 3.3, it was possible to evaluate the *SAR* values for the low, high and mid mass points, obtaining:

	Mass [kg]	Altitude [km]	SAR [km/kg]
High Mass point	36140	14.256	0.169
Low Mass point	28753	15.601	0.214
Mid Mass point	32446	14.822	0.189

Table 4.5: Mass-points and *SAR* values as in Annex 16 equations

As shown in figure 4.16, the points calculated according to the subsonic standard are not representative of the cruise condition.

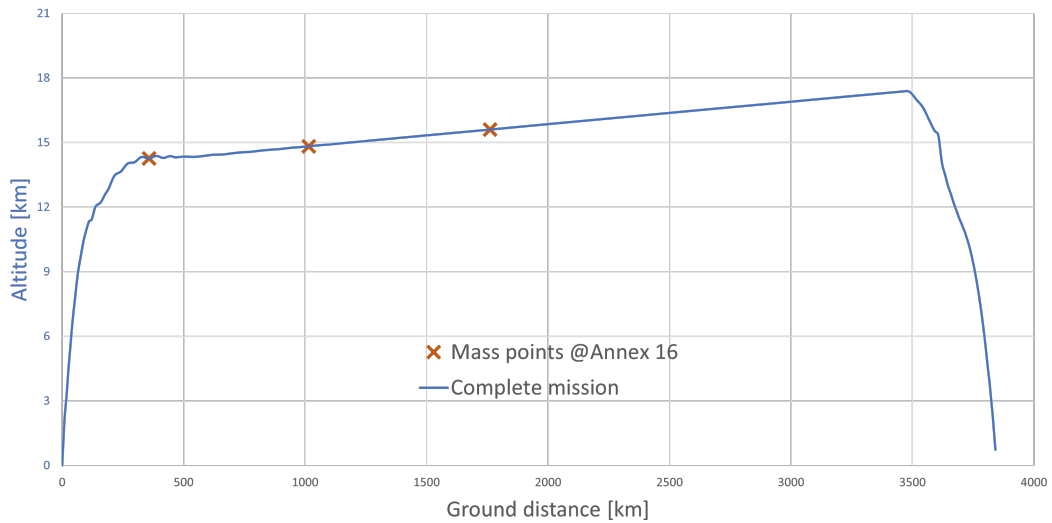


Figure 4.16: Mass-points as in Annex 16 equations

If the existing regulations are followed, the mid and low mass points are greatly overestimated, resulting in a much lighter aircraft than expected from the subsonic regulation at the end of the cruise. This result is in line with expectations since, compared to the subsonic case, it is reasonable to expect a higher fuel consumption for a supersonic cruise.

In order to make the mass points characteristic for the cruise condition, hence to keep valid the idea behind the regulation, a second *SAR* calculation was performed; in this condition, the reference equations for the high mass point and the low mass point vary as follows:

	High Mass point	Low Mass point
Regulation	$0.92 \cdot MTOM$	$(0.45 \cdot MTOM) + (0.63 \cdot MTOM^{0.924})$
Case study	$0.9196 \cdot MTOM$	$0.5547 \cdot MTOM$

Table 4.6: Reference equations variation

By representing these new points on the mission profile, it is possible to see how they are representative of the cruise condition, as presented in figure 4.17.

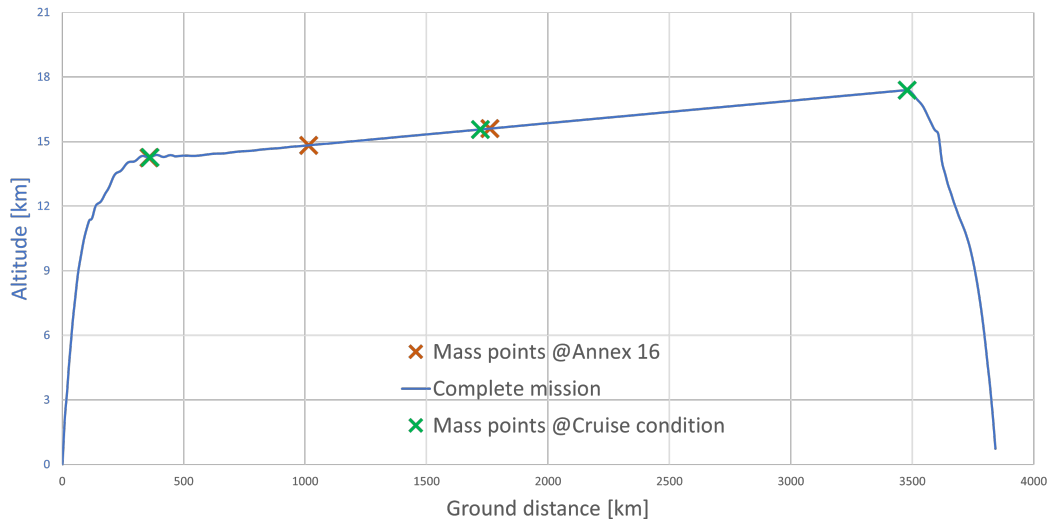


Figure 4.17: Mass-points at representative cruise condition

With reference to these modifications, it was possible to evaluate the *SAR* values for the mass points representative of the cruise condition, obtaining:

	Mass [kg]	Altitude [km]	SAR [km/kg]
High Mass point	36125	14.263	0.170
Low Mass point	21791	17.391	0.314
Mid Mass point	28958	15.561	0.213

Table 4.7: Mass-points and *SAR* values at cruise condition

In figure 4.18 the instantaneous SAR as function of the ground distance is presented:

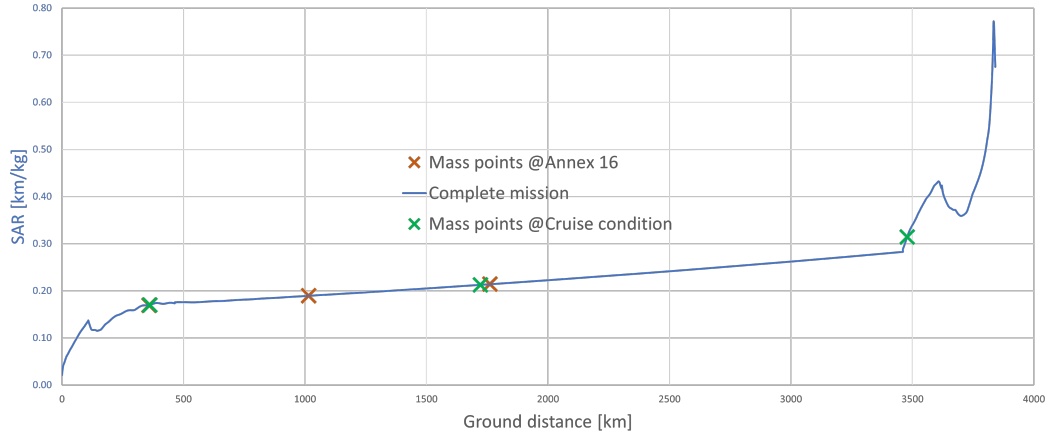


Figure 4.18: Instantaneous SAR

In order to calculate the CO_2 metric value, as shown in equation 4.7, the Reference Geometric Factor was derived.

$$CO_2 MV = \frac{1}{\frac{(SAR)_{avg}}{(RGF)^{0.24}}} \quad (4.7)$$

To evaluate the RGF , the area delimited by the maximum width of the fuselage and the length of the pressurised cabin, with the exception of the cockpit, was projected onto a plane parallel to the aircraft's axis X-body.



Figure 4.19: RGF evaluation: maximum width

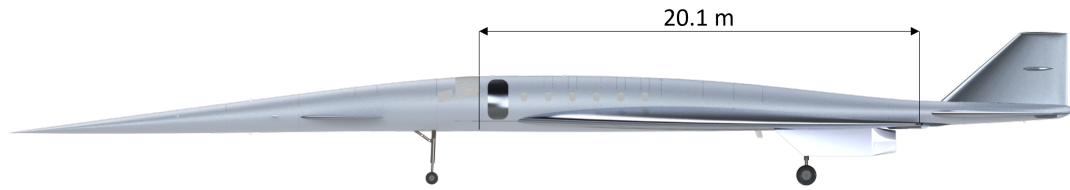


Figure 4.20: *RGF* evaluation: cabin length

Multiplying the quantities shown in figure 4.19 and 4.20, and normalizing the product to an area of 1 m^2 gives:

$$RGF = \frac{2.51 \text{ m} \cdot 20.1 \text{ m}}{1 \text{ m}^2} = 50.5 \quad (4.8)$$

Given this data, the work was concluded by evaluating the CO_2 metric value for the case study, as presented in figure 4.21, and in table 4.8.

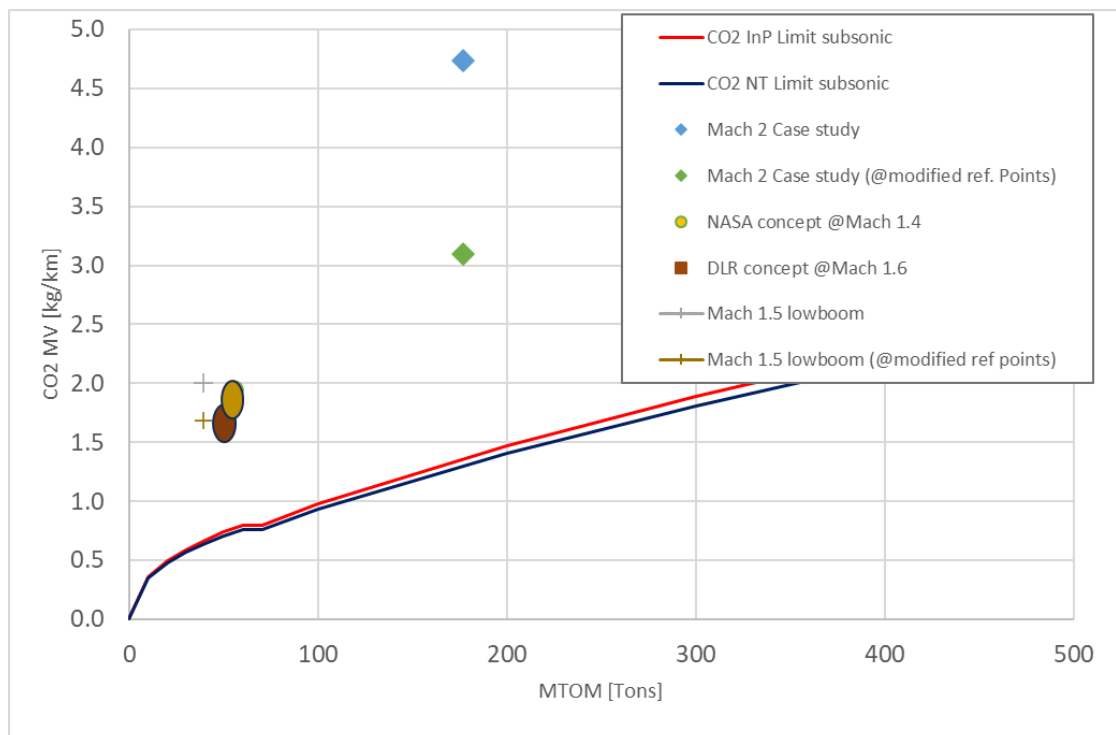


Figure 4.21: CO_2 metric value

	$(SAR)_{avg} [km/kg]$	RGF	$CO_2 MV [kg/km]$
Subsonic regulation	0.191	50.5	2.04
Supersonic modification	0.232	50.5	1.68

Table 4.8: $CO_2 MV$ results

These results are shown relative to the CO_2 limits for subsonic aircraft, and some additional points are also included from previous *NASA* Mach 1.4, *DLR* Mach 1.6, and Politecnico di Torino Mach 2.0 input into *CAEP-WG3* [56]. Also for this Mach 1.5 case study, the results fall short of the the subsonic norm by more than two times, even with modified reference points. This outcome, in the context of environmental impact, indicates a less favorable scenario for supersonic aviation, highlighting the substantial work that lies ahead in terms of sustainability and emissions reduction. However, what lends considerable strength and significance to this research, is the proximity of the results to those obtained by *NASA* and *DLR* for similar case studies. Furthermore, the chart also features two distinctive diamonds that represent a *PoliTo* Mach 2 case study, derived from the *Concorde* so way heavier than the presented business jet; even in this case, despite the disparity in the characteristics, the trend observed in the $CO_2 MV$ remains the same.

Chapter 5

Conclusions and future developments

The CO_2 metric value assessment of this conceptual design vehicle stands as one of the starting points for evaluating how subsonic regulations can be adapted to supersonic aircrafts, and represents an important step forward in understanding the environmental impact of the future supersonic aviation. This research has undertaken a comprehensive and multidisciplinary analysis, including an aerodynamic characterization and a mission simulation, to shed light on the potential for adapting subsonic regulation. This final chapter summarises the main results of the work and, for each section, presents some possible future developments.

Aircraft configuration As stated at the beginning of chapter 2, the aircraft results from the development of an high speed civilian vehicle, at a conceptual design stage, as part of an academic course. As mentioned earlier, its geometry derives from having proportionally enlarged the *NASA X-59* in order to accommodate the passengers, but further optimisation studies of the configuration were never carried out. Several studies may arise from this issue, in particular one promising future direction is to continue the study of the aircraft configuration with the aim of increasing its lift to drag ratio. By examining alternative designs, such as configurations without the canard, or with wider wing or tail surfaces, or even relocating the engines closer to the vertical tail, it is possible to obtain valuable insights into how different geometries impact the overall performance. Each configuration should undergo a comprehensive analysis, taking into account factors like aerodynamic stability, control effectiveness, and overall structural integrity, but also for each configuration, a set of studies analogous to those conducted for the original design should be presented.

In addition, it is worth noticing that, despite the vehicle derives from a low boom

configuration, the absence of an acoustic analysis is a big miss of the work. In this study, it is taken for granted that the aircraft can also fly over populated areas at cruising speed, thus exceeding the limits imposed by the regulations [18], however, it would be appropriate to improve the work by demonstrating this assumption.

Aerodynamic analysis The aerodynamic analysis conducted in this study serves as a cornerstone of the research, since it lays the foundations for the entire investigation into the CO_2 metric value. As stated in chapter 3, this analysis is of paramount importance as it provides the first crucial set of inputs for the subsequent mission simulation. The results obtained from this analysis align with expectations and offer valuable insights into the aircraft's performance. However, it's important to note that the simulations conducted were inviscid, representing an idealized scenario. To refine the results and to ensure a more accurate representation of real-world conditions, future works should consider the reassessment of the test matrix through viscous simulations.

Revisiting the analysis with viscous simulations will not only yield more precise data, but will also provide an opportunity to assess the effectiveness of the viscous correction used earlier, presenting an opportunity to better tune the coefficients α, β and γ . This iterative approach can be used to validate the accuracy of the correction and, eventually, to make necessary adjustments. Moreover, other studies including the investigation of control surfaces should be faced. For example, by conducting simulations with various aileron deflection at different Mach number, a deeper understanding of the control capabilities of the aircraft can be gained.

Mission simulation The mission simulation conducted in this project plays a crucial role in understanding how certain quantities and parameters of the aircraft vary throughout the mission, hence in the assessment of the CO_2 metric value. As previously mentioned in chapter 3, this simulation process relies on two fundamental inputs: the aerodynamic database, and the propulsion database. In this specific case, the aircraft is equipped with two state-of-the-art turbofan engines at the conceptual design stage, therefore an important lack of data to generate a propulsion database was faced. The problem has been overcome thanks to my colleague Francesco [1] who developed an algorithm to estimate some critical engine parameters. Although his results are in line with expectation, there remains room for refinement and improvement in the accuracy of the model. For this reason, future work in this domain should prioritize the development of an enhanced propulsion database, so as to lead to a more accurate environmental assessment.

Additionally, the *ASTOS* software employed offers a wide range of capabilities, including trajectory optimization. Exploring this functionality presents another interesting idea of future developments, because it could identify a better mission

profile in order to search for additional opportunities to reduce fuel consumption, minimize emissions, and enhance overall environmental performance.

CO_2 Metric Value The main goal of this thesis was the assessment of the CO_2 metric value of the case study and it has been conducted. This investigation stands as one of the first studies on the importance to adapt and apply existing subsonic regulations to supersonic aircrafts, acknowledging the crucial need for sustainable aviation practices in the supersonic future. The CO_2 metric value of this vehicle exceeds the limits permitted by current subsonic regulations, with an impact approximately twice that of subsonic aircraft limitations. While this outcome underscores the environmental implications of supersonic aviation, it's noteworthy that the results obtained in this research align closely with those reported by *NASA* and *DLR* on similar case studies. This convergence highlights the credibility and robustness of the presented findings.

As part of future works, one promising direction could involve the evaluation of sustainable aviation fuels (*SAFs*) as a component of the CO_2 metric value assessment. Although the aircraft does not respect subsonic limitations, assessing the potential benefits of biofuels in reducing emissions and the carbon footprint, could be the key to making supersonic passenger flight possible.

Additionally, further studies should focus onto the reference geometric factor and its role in the CO_2 *MV* assessment.

Furthermore, a comprehensive array of case studies at various Mach numbers should be undertaken to gather a huge dataset. This data will provide insights into the behavior of supersonic vehicles under different conditions and help determine the feasibility of modifying current subsonic regulations to accommodate the specificities of supersonic flight, contributing to a more informed approach to supersonic aviation.

In conclusion, this thesis has made a small contribution to the evaluation of the CO_2 metric value for a supersonic business jet, but a lot of works still needs to be done, with the aim of shaping a supersonic yet sustainable future.

Bibliography

- [1] Francesco Piccionello. «Modeling of Propulsion Systems for Supersonic Civil Aircraft». MA thesis. Torino: Politecnico di Torino, 2023 (cit. on pp. ii, 22, 29, 46, 73).
- [2] *2022 Environmental Report*. 999 Robert-Bourassa Boulevard Montreal, QC, Canada H3C 5H7: ICAO, 2022 (cit. on pp. iii, 8, 10).
- [3] U.S. Air Force Biography. *Brigadier General Chuck Yeager*. Huntington, West Virginia: Digitized Manuscript Collections 1923-1987, 1973 (cit. on p. 1).
- [4] Preston A. Henne. «Case for Small Supersonic Civil Aircraft». In: *JOURNAL OF AIRCRAFT* 42 (May 2005) (cit. on pp. 2, 12).
- [5] Howard Smith Yicheng Sun. «Review and prospect of supersonic business jet design». In: *Progress in Aerospace Sciences* 90 (2017), pp. 12–38 (cit. on pp. 1, 4, 12, 14, 15).
- [6] Richard Seebass. *History and Economics of, and Prospects for, Commercial Supersonic Transport*. Tech. rep. Boulder CO, USA: University of Colorado, May 1998 (cit. on pp. 2, 3).
- [7] Anuradha Das Umesh Siddarth. «A review study on supersonic flight». In: *International Journal of Engineering Applied Sciences and Technology* 2 (Feb. 2017) (cit. on p. 2).
- [8] Julien Chicot Alberto Domini. *From Concorde to Airbus*. Tech. rep. B-1049 Brussels: European Commission, Feb. 2018 (cit. on p. 3).
- [9] Adrian Meredith. PhD thesis. Irish Sea: Royal Air Force (RAF), Apr. 1985. URL: <https://theaviationgeekclub.com/heres-the-only-picture-of-concorde-flying-at-supersonic-speed/> (cit. on p. 3).
- [10] Robert Curley. *The complete history of aviation: from ballooning to supersonic flight*. 29 East 21 st Street, New York, NY 10010: Britannica Educational Publishing in collaboration with Rosen Educational Services, 2012 (cit. on p. 5).
- [11] Dietrich Küchemann. *The Aerodynamic Design of Aircraft*. American Institute of Aeronautics and Astronautics, 2012 (cit. on p. 5).

- [12] Jericho W. Locke Sara A. Carioscia. *Commercial Development of Civilian Supersonic Aircraft*. Institute for Defense Analyses, 2019 (cit. on p. 6).
- [13] Alain Bernard Dervieux Mariano Vázquez. PhD thesis. 08034 Barcelona, Spain: Barcelona Supercomputing Center, June 2006. URL: <https://www.researchgate.net/publication/235274538/figure/fig6/AS:668846054727681@1536476734065/The-sonic-boom-simplified-case-of-a-N-wave-Sketch-of-near-and-far-field-shock-wave.png> (cit. on p. 6).
- [14] Samuele Graziani. «Sensitivity analysis for sonic boom phenomena for different type of supersonic aircraft». PhD thesis. Politecnico di Torino, Oct. 2021 (cit. on p. 6).
- [15] William E. Schiesser Graham W Griffiths. PhD thesis. London, United Kingdom: City, University of London, Jan. 2009. URL: <https://www.researchgate.net/publication/220579728/figure/fig11/AS:305597107982338@1449871436097/The-N-wave-sonic-boom-Nak-08.png> (cit. on p. 7).
- [16] Vera Huckel David A. Hilton. *Sonic-boom exposures during FAA community-response studies over a 6-month period in the oklahoma city area*. Tech. rep. Langley Station, Hampton, Va.: Langley Research Center, Dec. 1964 (cit. on p. 7).
- [17] K. Lütjens B. Liebhardt. «Analysis of the market environment for supersonic business jets». In: German Aerospace Center (DLR), Jan. 2011 (cit. on pp. 7, 12).
- [18] FAA. *14 CFR Part 91.817*. Tech. rep. Federal Aviation Administration, 1973 (cit. on pp. 7, 73).
- [19] Fuel Cells and Hydrogen 2 Joint Undertaking. *Hydrogen-powered aviation : a fact-based study of hydrogen technology, economics, and climate impact by 2050*. Publications Office, 2020. DOI: [doi/10.2843/471510](https://doi.org/10.2843/471510) (cit. on pp. 9–11).
- [20] Dan Rutherford Anastasia Kharina Tim MacDonald. «Environmental performance of emerging supersonic transport aircraft». In: *The International Council on Clean Transportation*. Dec. 2018 (cit. on p. 10).
- [21] PhD thesis. Miami Gardens, FL: Meridian International Research, 1999. URL: <http://www.meridian-int-res.com/Projects/PrevProjects.htm#SSBJ1> (cit. on p. 12).
- [22] C. Trautvetter. «Viable Market for SSBJ». PhD thesis. 5190 Neil Rd, Reno: Aerion Corporation, Oct. 2006 (cit. on p. 12).
- [23] John Wiley. «The Super-Slow Emergence of Supersonic». PhD thesis. Aviation Week, Sept. 2007 (cit. on p. 12).

- [24] Domenic J. Maglieri. *Compilation and Review of Supersonic Business Jet Studies from 1963 through 1995*. Tech. rep. Hampton, Virginia: Eagle Aeronautics, Inc., May 2011 (cit. on p. 12).
- [25] J. Bonet H. Welge C. Nelson. «Supersonic vehicle systems for the 2020–2035 timeframe». In: *AIAA 2010-4930, 28th AIAA Applied Aerodynamics Conference*. Chicago, Illinois, May 2010 (cit. on p. 13).
- [26] Sean O’Neill. «Supersonic Travel Seeks an Encore». In: *Engineering* 10 (Feb. 2022) (cit. on p. 14).
- [27] Eric Hagerman. *All Sonic, No Boom*. Mar. 2007. URL: <https://web.archive.org/web/20070214074550/http://www.popsci.com/popsci/aviationspace/511395ca8c6a0110vgnvcm1000004eecbccdrord.html> (cit. on p. 14).
- [28] Sylvie Peron. «The QSST-X Program». In: *Latitudes Magazine* (Jan. 2014) (cit. on p. 14).
- [29] Spike Aerospace. *Enjoy Life With The Spike S-512*. URL: <https://www.spikeaerospace.com/portfolio-items/enjoy-life-with-the-spike-s-512/?portfolioCats=130%2C131%2C132> (cit. on p. 15).
- [30] Octuri. URL: <https://www.octuri.com/en/aircraft-for-today/sonicstar/> (cit. on p. 15).
- [31] Jonathan Rathsam. «Scope and goals of NASA’s Quesst Community Test Campaign with the X-59 aircraft». In: *14th IC BEN Congress on Noise as a Public Health Problem* (June 2023) (cit. on p. 16).
- [32] Don Durston. «NASA Supersonics Research —Leading Toward Quiet Supersonic Flight!!» In: *EAA AirVenture*. June 2022 (cit. on p. 16).
- [33] L. R. Benson. *Quieting The Boom*. NASA Aeronautics book series, 2013 (cit. on p. 18).
- [34] Y. Sun and H. Smith Yicheng Sun. «Low-boom low-drag solutions through the evaluation of different supersonic business jet concepts». In: 124 (2020), pp. 76–76. DOI: 10.1017/aer.2019.131. URL: <https://doi.org/10.1017/aer.2019.131> (cit. on pp. 18, 19).
- [35] Michał Wojcieszuk Yuri Kroyan. «Modeling the impact of sustainable aviation fuel properties on end-use performance and emissions in aircraft jet engine». In: *Energy* (June 2021) (cit. on p. 20).
- [36] Airbus. URL: <https://www.travelweekly-asia.com/Travel-News/Airline-News/Across-the-globe-airlines-are-in-haste-for-waste> (cit. on p. 20).
- [37] Michał Wojcieszuk Yuri Kroyan. «Modeling the impact of sustainable aviation fuel properties on end use performance and emissions in aircraft jet engine». In: 255 (2022) (cit. on pp. 20, 21).

- [38] Marco Debiasi. «Conceptual Development of Quiet Turbofan Engines for Supersonic Aircraft». In: *Journal of Propulsion and Power* (Mar. 2003) (cit. on pp. 21, 22).
- [39] T. Astarita. «Propulsione Aerospaziale». In: 2020. URL: <http://wpage.unina.it/astarita/Corsi/PA/PA2%20Spinta%20e%20prestazioni.pdf> (cit. on p. 22).
- [40] Map Developers. URL: <https://www.mapdevelopers.com/draw-circle-tool.php> (cit. on p. 23).
- [41] Ray Castner. «NQuiet Supersonic Technology (X-59 QueSST) X-Plane Testing, Analysis, and Progress». In: *NASA Glenn Research Center*. Cleveland OH, Apr. 2022 (cit. on p. 24).
- [42] Dieter Scholz. *ICAO Annex 16 - Environmental Protection — Volume III - CO2 Certification Requirement*. Version V1. 2021. DOI: 10.7910/DVN/FFQPEP. URL: <https://doi.org/10.7910/DVN/FFQPEP> (cit. on pp. 29, 48–51).
- [43] M. Perić J. Ferziger. *Computational Methods for Fluid Dynamics*. Berlin: Springer, 1999 (cit. on pp. 30, 38, 44).
- [44] Renzo Arina. *Fondamenti di Aerodinamica*. Torino: Levrotto e Bella, 2019 (cit. on p. 30).
- [45] Inc ANSYS. *Ansys Fluent Theory Guide*. 2600 Ansys Drive Canonsburg, PA 15317: Southpointe, 2021 (cit. on pp. 36, 42).
- [46] Dario De Luca. «Sub-Transonic and Supersonic STRATOFly MR3 Aerodatabase development by means of CFD Simulations». MA thesis. Torino: Politecnico di Torino, 2020 (cit. on p. 37).
- [47] Inc ANSYS. *Ansys ICEM CFD User's Manual*. 2600 Ansys Drive Canonsburg, PA 15317: Southpointe, 2021 (cit. on p. 38).
- [48] Inc ANSYS. *ANSYS ICEM CFD Tutorial Manual*. 275 Technology Drive Canonsburg, PA 15317: Southpointe, 2012 (cit. on p. 39).
- [49] Inc ANSYS. *Ansys Fluent User's Guide*. 275 Technology Drive Canonsburg, PA 15317: Southpointe, 2010 (cit. on pp. 43, 44).
- [50] Andrew Wood. *Standard Atmosphere Calculator*. Sept. 2022. URL: <https://aerotoolbox.com/atmcalc/> (cit. on pp. 44, 50).
- [51] Francesco Cremaschi, Sven Weikert, Andreas Wiegand, Wolfgang Jung, and Frank Scheuerpflug. «Sounding rocket trajectory simulation and optimization with astos». In: 2009. URL: <https://api.semanticscholar.org/CorpusID:53064719> (cit. on p. 46).

- [52] Francesco Cremaschi. «Analysis, Simulation and Trajectory optimisation for Space Scenarios (ASTOS) Market-Oriented Activities». In: 2017. URL: <https://www.astos.de/download?TYPE=PAPER&ID=15> (cit. on p. 46).
- [53] International Civil Aviation Organization. *Climate Change Technology Standards*. 2017. URL: https://www.icao.int/environmental-protection/Pages/ClimateChange_TechnologyStandards.aspx (cit. on p. 48).
- [54] *Environmental protection requirements for supersonic transport aeroplanes*. 2022. URL: <https://www.easa.europa.eu/en/downloads/136561/en> (cit. on pp. 49, 50).
- [55] Nicole Viola, Pietro Roncioni, Oscar Gori, and Roberta Fusaro. «Aerodynamic Characterization of Hypersonic Transportation Systems and Its Impact on Mission Analysis». In: *Energies* 14.12 (2021). ISSN: 1996-1073. DOI: 10.3390/en14123580. URL: <https://www.mdpi.com/1996-1073/14/12/3580> (cit. on p. 56).
- [56] International Civil Aviation Organization. *Committee on Aviation Environmental Protection Working Group 3*. URL: <https://www.icao.int/environmental-protection/Pages/CAEP-WG3.aspx> (cit. on p. 71).